

Endogenous self-peptides guard immune privilege of the central nervous system

<https://doi.org/10.1038/s41586-024-08279-y>

Received: 15 August 2023

Accepted: 23 October 2024

Published online: 30 October 2024

Open access

 Check for updates

Min Woo Kim^{1,2,3,4}, Wenqing Gao^{1,2}, Cheryl F. Lichti^{1,2,5}, Xingxing Gu^{1,2}, Taitea Dykstra^{1,2}, Jay Cao^{1,2}, Igor Smirnov^{1,2}, Pavle Boskovic^{1,2}, Denis Kleverov^{2,6}, Andrea F. M. Salvador^{1,2}, Antoine Drieu^{1,2}, Kyungdeok Kim^{1,2}, Susan Blackburn^{1,2}, Clair Crewe⁷, Maxim N. Artyomov^{2,5}, Emil R. Unanue^{1,2,5,8} & Jonathan Kipnis^{1,2,5,9}

Despite the presence of strategically positioned anatomical barriers designed to protect the central nervous system (CNS), it is not entirely isolated from the immune system^{1,2}. In fact, it remains physically connected to, and can be influenced by, the peripheral immune system¹. How the CNS retains such responsiveness while maintaining an immunologically unique status remains an outstanding question. Here, in searching for molecular cues that derive from the CNS and enable its direct communication with the immune system, we identified an endogenous repertoire of CNS-derived regulatory self-peptides presented on major histocompatibility complex class II (MHC-II) molecules in the CNS and at its borders. During homeostasis, these regulatory self-peptides were found to be bound to MHC-II molecules throughout the path of lymphatic drainage from the brain to its surrounding meninges and its draining cervical lymph nodes. However, in neuroinflammatory disease, the presentation of regulatory self-peptides diminished. After boosting the presentation of these regulatory self-peptides, a population of suppressor CD4⁺ T cells was expanded, controlling CNS autoimmunity in a CTLA-4- and TGFβ-dependent manner. CNS-derived regulatory self-peptides may be the molecular key to ensuring a continuous dialogue between the CNS and the immune system while balancing overt autoreactivity. This sheds light on how we conceptually think about and therapeutically target neuroinflammatory and neurodegenerative diseases.

For a long time, the concept of immune privilege solidified a framework through which the interaction between the CNS and the periphery was understood. Given the ability of the CNS to tolerate the transplantation of autologous grafts or sarcomas^{3–5}, it was widely presumed that the brain walled itself off from the peripheral immune system⁶. While the presence of physical barriers in the brain, together with its perceived lack of lymphatic drainage, was thought to help the CNS sustain its immune-privileged nature, the identification of a bona fide lymphatic network at the brain borders began to break down this supposed disconnect from the peripheral immune system^{7,8}. In fact, juxtaposed with an immunologically frugal brain parenchyma, there is an immunologically rich niche of immune cells in the brain meninges, especially in the dura mater—the outermost membranous covering that envelops the CNS^{9,10}.

Moreover, recent work has demonstrated the accessibility of CNS-derived antigens within these neuroimmune hubs, potentiating their presentation on MHC-II molecules to circulating self-reactive T cells⁹. Indeed, more than 30 years ago, the presence of circulating autoreactive T cells, even in healthy individuals, was reported¹¹. Thus, although it is by now well accepted that autoreactive CD4⁺ T cells provoke autoimmune disease, their potentially beneficial roles across an

array of diseases and in the normal functioning of the CNS have only more recently been appreciated^{12–14}. This raises the question of how the CNS maintains immune tolerance while enhancing its visibility to the immune system, and of whether the CNS seeks immunosurveillance while actively providing immune cells with molecular cues to foster its tolerance to autoreactivity.

To begin examining plausible molecular cues coming from the CNS to its patrolling CD4⁺ T cells, we performed a thorough examination of the CNS, its borders and its draining lymph nodes (LNs) for peptides bound to MHC-II molecules. In establishing the MHC-II peptidome of the CNS, we found CNS-derived regulatory self-peptides. These self-antigens were identified on MHC-II molecules in homeostasis and evoked immunosuppressive CD4⁺ T cells, which controlled CNS autoimmunity through CTLA-4 and TGFβ. We further showed that not all professional antigen-presenting cells (APCs) shared the same capacity to present these regulatory self-peptides and that inflammation-mediated alterations to antigen processing mechanisms resulted in a marked decrease in their presentation. However, their restoration sufficiently ameliorated neuroinflammatory disease. Together, we demonstrate that the CNS presents select endogenous self-peptides on MHC-II molecules

¹Brain Immunology and Glia (BIG) Center, School of Medicine, Washington University in St Louis, St Louis, MO, USA. ²Department of Pathology and Immunology, School of Medicine, Washington University in St Louis, St Louis, MO, USA. ³Immunology Graduate Program, School of Medicine, Washington University in St Louis, St Louis, MO, USA. ⁴Medical Scientist Training Program, School of Medicine, Washington University in St Louis, St Louis, MO, USA. ⁵Bursky Center for Human Immunology and Immunotherapy Programs, School of Medicine, Washington University in St Louis, St Louis, MO, USA. ⁶Computer Technologies Laboratory, ITMO University, Saint Petersburg, Russia. ⁷Department of Cell Biology and Physiology, School of Medicine, Washington University in St Louis, St Louis, MO, USA. ⁸Deceased: Emil R. Unanue. [✉]e-mail: kipnis@wustl.edu

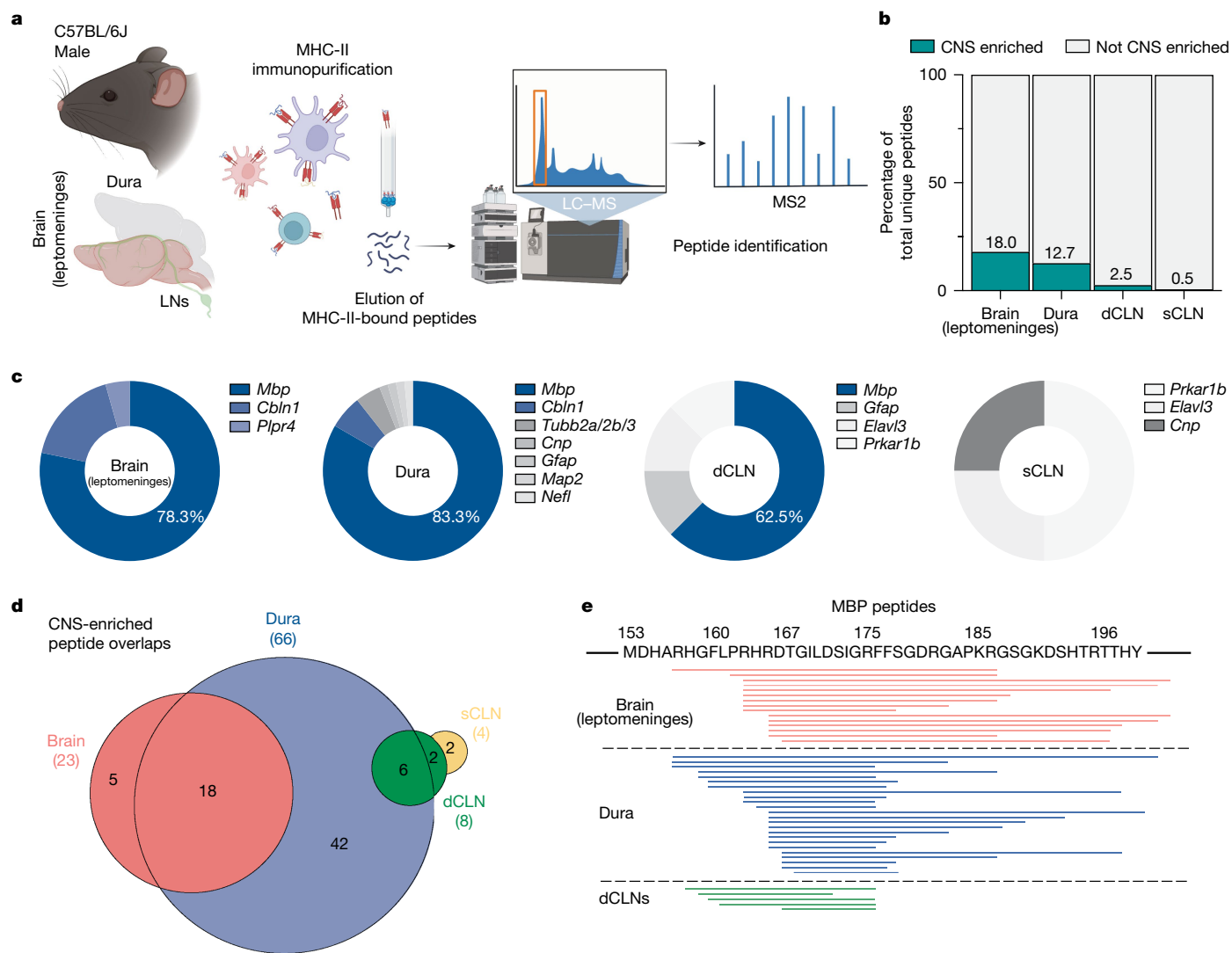


Fig. 1 | The CNS MHC-II peptidome reveals presentation of endogenous CNS peptides. **a**, Schematic of MS identification of MHC-II-bound peptides from the brain (including leptomeninges), dural meninges (dura) and LNs, including the dCLNs and sCLNs, of C57BL/6J male mice. The diagram was created with BioRender.com. **b**, The proportion of total unique identified peptides that could be designated as CNS enriched (teal bar); percentages are indicated

above each individual bar. **c**, CNS-enriched, MHC-II-bound peptides identified for each individual tissue. The percentage composed by MBP is indicated where relevant. **d**, The relationship between CNS-enriched, MHC-II-bound peptides in the brain, dura, dCLNs and sCLNs. **e**, Summary of individual peptide sequences contained within the MBP_{158–195} region as defined by the MHC-II peptidome.

to communicate with and dampen autoreactive T cell responses to secure CNS immunosurveillance.

CNS self-peptides in the MHC-II peptidome

Driven by the hypothesis that the CNS may use the presentation of antigens to control the immune system during homeostasis, we began our study by investigating the repertoire of antigens presented on MHC-II molecules. To address this question, we performed mass spectrometry (MS) to comprehensively evaluate the CNS and its associated tissues for peptides bound to MHC-II molecules in C57BL/6J male mice (Fig. 1a). We found that CD11b⁺CD11c⁻ macrophages were the predominant MHC-II-expressing APCs in the brain, which also includes the leptomeninges and the dura, whereas CD19⁺ B cells were the main APCs in the deep cervical LNs (dCLNs) and in the superficial cervical LNs (sCLNs) (Extended Data Fig. 1a–e). Moreover, algorithmic predictions of MHC-II-binding affinities using three independent models^{15–17} identified a propensity for peptides with relatively weaker affinities to be bound to MHC-II molecules in the brain. By contrast,

further downstream along the path of lymphatic drainage, peptide binding affinities increased, suggesting that there is heterogeneity in the repertoire of peptides bound to MHC-II molecules in different compartments (Extended Data Fig. 1f).

We next took advantage of published transcriptomic data of mammalian brains¹⁸ to distinguish peptides derived from proteins of which the expression in the CNS was enriched. We found that 18.0%, 12.7%, 2.5% and 0.5% of total MHC-II-bound peptides in the brain (including leptomeninges), dura, dCLNs and sCLNs, respectively, could be annotated as CNS enriched (Fig. 1b). Analysis of the repertoire of CNS-enriched autoantigens across the different tissues revealed an abundance of peptides derived from myelin basic protein (MBP) in the brain, dura and dCLNs, and their apparent absence in the sCLNs (Fig. 1c). By comparing overlapping peptide sequences between tissues, we further validated that the dCLNs are the major route for lymphatic drainage from the brain during homeostasis^{19,20} (Fig. 1d and Extended Data Fig. 1g). Furthermore, alignment of the amino acid sequences for the different MBP peptides identified across the brain, the dura and the dCLNs highlighted two distinct regions, namely MBP_{158–195} and MBP_{196–236}

Article

(Fig. 1e and Extended Data Fig. 1h). The vast majority of MHC-II-bound MBP peptides were contained within the upstream MBP_{158–195} sequence, representing the main region draining to the dCLNs (Extended Data Fig. 1h).

We repeated these experiments in C57BL/6J female and SJL/J male mice. As compared with C57BL/6J male mice, C57BL/6J female mice exhibited an abundance of MBP peptides bound to MHC-II molecules in the brain as well as in the dura (Extended Data Fig. 2a). Moreover, there was a similar over-representation of MHC-II-bound peptides encompassing the MBP_{158–195} region in comparison to the MBP_{196–236} region in C57BL/6J female mice as well (Extended Data Fig. 2b). Indeed, a considerable amount of identical CNS-enriched peptide sequences was found to be shared between C57BL/6J female and male mice, both in the brain and in the dural meninges (Extended Data Fig. 2c–f). Upon evaluating the immunopeptidome of SJL/J male mice, we also observed MHC-II-bound peptides with relatively weaker binding affinities in the brain that increased towards the draining LNs, further reiterating that endogenous antigens with different characteristics bound to MHC-II molecules in the brain and dura in comparison to those bound to MHC-II in the draining LNs (Extended Data Fig. 3a). Moreover, similar to C57BL/6J mice, we observed a heightened presentation of CNS-enriched self-antigens in the dural meninges (Extended Data Fig. 3b–d). However, in contrast to C57BL/6J mice, the diversity of CNS-enriched proteins bound to MHC-II molecules was increased in the SJL/J mice, with MHC-II molecules also displaying peptides derived from neurofilaments, microtubule-associated proteins and β -synuclein, among others (Extended Data Fig. 3e). Despite this increased diversity, peptides comprising the same MBP_{158–195} and MBP_{196–236} regions as those found in C57BL/6J mice could still be identified in both the brain and the dural meninges of SJL/J mice (Extended Data Fig. 3e,f). Collectively, these data demonstrated marked conservation with respect to the presentation of MBP-derived peptides on MHC-II molecules in the CNS (Supplementary Table 1).

MBP peptides suppress immune responses

We began screening identified MBP peptides by immunizing mice with the peptides to assess their encephalitogenicity. Whereas immunization of mice with myelin oligodendrocyte glycoprotein (MOG)_{35–55} induced paralysis typical of experimental autoimmune encephalomyelitis (EAE)²¹—a mouse model of multiple sclerosis (MS)^{22,23}—immunization with endogenous MBP peptides, such as MBP_{160–175}, did not induce paralysis (Fig. 2a). As expected, these findings were consistent with previous observations that the C57BL/6J strain is particularly resistant to MBP-induced EAE²⁴. When we compared their draining LNs after immunization, mice that had received MBP_{160–175} peptides exhibited decreased cellularity relative to those that were immunized with MOG_{35–55} peptides (Fig. 2b). Moreover, MBP_{160–175}, in contrast to MOG_{35–55}, lacked an antigen-specific effector T cell response when assaying for IL-2 production using enzyme-linked immunosorbent spot (ELISpot) (Fig. 2c). To determine whether the low immunogenicity of MBP_{160–175} was specific to this particular peptide, we further tested different MBP peptides identified by the immunopeptidome. Immunization with MBP_{166–185}, a peptide contained within the MBP_{158–195} region, also showed a lack of IL-2 production similar to that seen for MBP_{160–175} (Extended Data Fig. 4a,b). By contrast, immunization with MBP_{192–216} elicited an activated T cell response (Extended Data Fig. 4a,b).

On the basis of the above findings, we wondered whether MBP peptides within the MBP_{158–195} region might serve to give rise to more suppressive T cells and therefore dampen the immune response. To test that possibility, we co-immunized mice with encephalitogenic MOG_{35–55} peptide and endogenous MBP peptides. Co-immunization of MOG_{35–55} peptide with either MBP_{160–175} or MBP_{166–185}, but not with MBP_{192–216}, significantly attenuated the neuroinflammatory disease (Fig. 2d and Extended Data Fig. 4c). To ascertain that peptide specificity

had a role in the observed protection, we directly modified the MBP_{160–175} sequence by converting its arginine residues to citrulline. Citrullination has been implicated in a variety of autoimmune diseases, and studies have demonstrated that MBP itself becomes hypercitrullinated and that this correlates with increased disease severity in both multiple sclerosis and EAE^{25,26}. We found that citrullinated MBP_{160–175} (MBP_{160–175(cit)}), when co-immunized with MOG_{35–55}, indeed no longer suppressed EAE, implying a specific immunomodulatory function for naked MBP_{160–175} peptides in regulating neuroinflammation (Fig. 2d). We further evaluated whether citrullination affected the ability of MBP_{160–175} peptides to bind to MHC-II and found that MBP_{160–175(cit)} peptides actually exhibited higher relative binding affinities to MHC-II compared with unmodified MBP_{160–175} peptides (Extended Data Fig. 4d). Moreover, the specific immunosuppression of neuroinflammatory disease with MBP_{160–175} peptides could be observed both in C57BL/6J female mice and in another model of active EAE with SJL/J male mice induced by proteolipid protein (PLP) immunization (Extended Data Fig. 4e,f).

Having observed a more pronounced protection with MBP_{160–175}, we focused on this particular peptide to determine potential mechanisms for its immunosuppression. To begin investigating the T cell phenotype elicited in the presence of MBP_{160–175}, we individually sorted for T cells from the draining inguinal LNs (iLNs) of the MOG_{35–55}-only and the MOG_{35–55} + MBP_{160–175} immunization groups, and then performed single-cell RNA sequencing (scRNA-seq) analysis using the 10x Genomics Chromium gene expression platform. We then conducted unsupervised clustering and dimensionality reduction to project the cells into two dimensions using the uniform manifold approximation and projection (UMAP) algorithm. Differential gene expression resolved 15 distinct clusters by which CD4⁺ T cells and CD8⁺ T cells could be distinguished (Fig. 2e and Extended Data Fig. 5a). By comparing the distribution of the identified clusters between the MOG_{35–55} and MOG_{35–55} + MBP_{160–175} groups, we observed differences in regulatory FOXP3⁺CD4⁺ T cells and activated CXCR3⁺CCL5⁺CD8⁺ T cells, both of which have been described to have implications in autoimmune diseases, including multiple sclerosis^{27–29}. Notably, with MOG_{35–55} + MBP_{160–175} co-immunization, the frequency of regulatory CD4⁺ T cells increased significantly, with evident attenuation in the CXCR3⁺CCL5⁺CD8⁺ T cell cluster (Fig. 2f). These observations were consistent with Gene Ontology (GO) analysis that revealed upregulated pathways, such as negative regulation of T cell activation and proliferation as well as enhanced inhibitory cytokine (IL-10 and TGF β) production, in the MOG_{35–55} + MBP_{160–175} group (Fig. 2g). Together, scRNA-seq analysis of both CD4⁺ and CD8⁺ T cells suggested that changes induced by MBP_{160–175} were already occurring in the draining LNs before the onset of EAE, shaping the immune response towards that of suppression.

Concordant with the scRNA-seq data, the population of FOXP3⁺CD4⁺ regulatory T cells remained increased both in the draining LNs and in the dCLNs at the onset of EAE after co-immunization of MBP_{160–175} relative to the MOG_{35–55} group (Fig. 2h,i and Extended Data Fig. 5b–e). We also noted that, in the MBP_{160–175} co-immunized group, there was a significant increase in a CTLA-4⁺FOXP3[−]CD4⁺ T cell population that expanded both in the dCLNs and in the spinal cord (Fig. 2h–k). In fact, this same T cell population in the MBP_{160–175} co-immunized group also demonstrated increased CD39 expression in the spinal cord, suggesting that the anti-inflammatory activity of this population functions, in part, through the depletion of extracellular ATP³⁰ (Fig. 2j,k). Furthermore, the immunosuppressive phenotype supported by MBP_{160–175} co-immunization persisted during disease resolution, as the dural meninges of both the brain and spinal cord exhibited heightened levels of FOXP3⁺CD4⁺ regulatory T cells (Extended Data Fig. 5f–i).

To determine whether MBP-specific CD4⁺ T cells directly contributed to the aforementioned increase in the regulatory pool of CD4⁺ T cells, we sought to develop MHC-II tetramers that would permit their identification in vivo. By generating MBP-specific hybridomas, we first narrowed down the binding core to MBP_{166–175}, which was

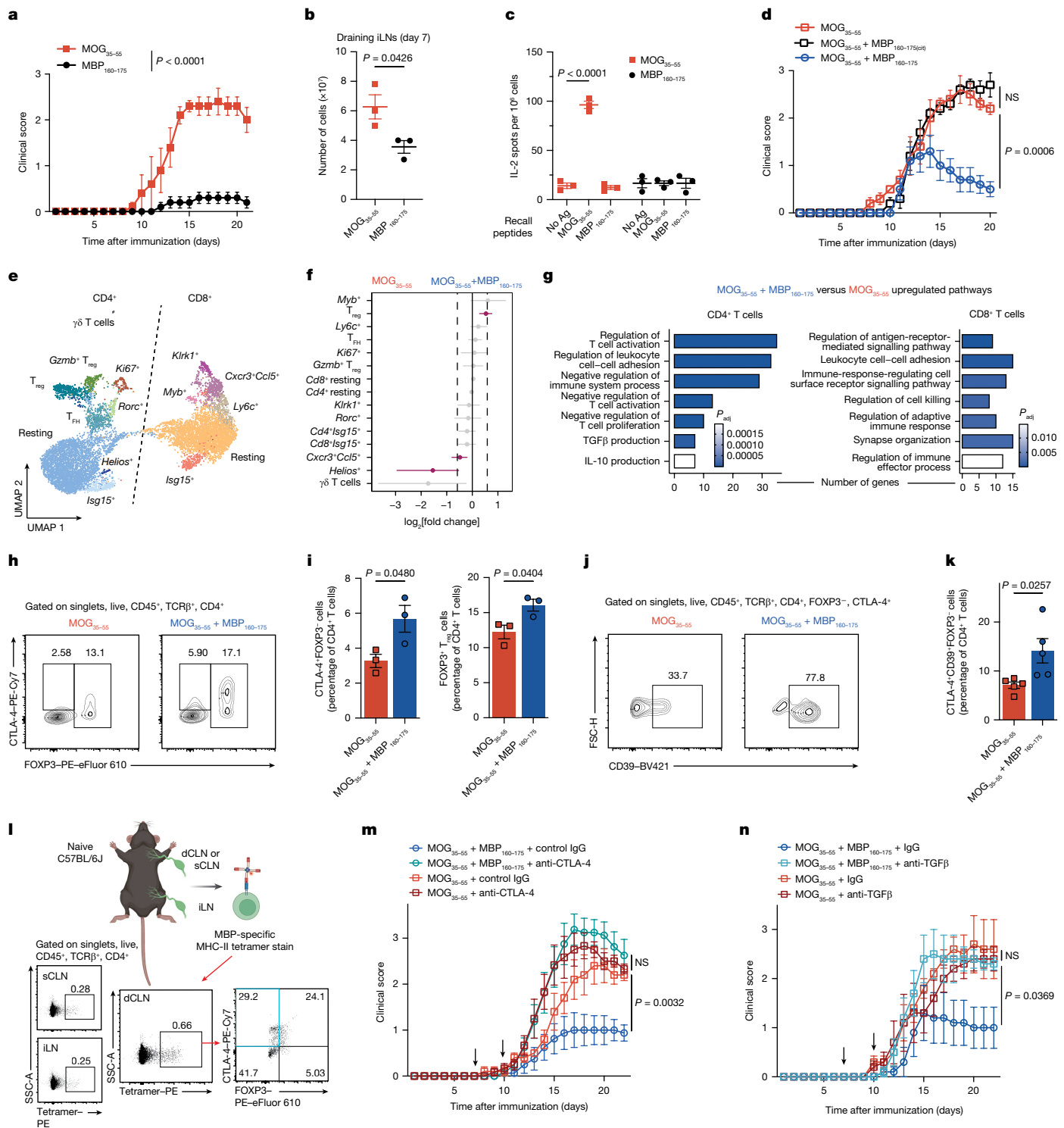


Fig. 2 | See next page for caption.

featured in the vast majority of MBP peptides found in the MHC-II peptidome of the CNS and its associated immune structures (Fig. 1e and Extended Data Fig. 6a). Identification of the binding core assisted in the development of MBP-specific MHC-II tetramers. Next, using our developed MHC-II tetramers, we distinguished MBP-specific CD4⁺ T cells in the draining LNs to the site of immunization; a fraction of them phenotypically labelled as conventional FOXP3⁺ regulatory T cells, but a more prominent population stained FOXP3⁻CTLA-4⁺, and many of which also expressed TGF β (Extended Data Fig. 6b).

Then, by performing scRNA-seq analysis of MBP-tetramer-positive and MBP-tetramer-negative CD4⁺ T cells from the draining iLNs, we observed enrichment and clonal expansion to CD4⁺ T cells exhibiting a regulatory phenotype with significant increases in the expression of both *Tgfb1* and *Ctla4* (Extended Data Fig. 6c–g). Moreover, in naive C57BL/6J mice, we identified MBP-specific CD4⁺ T cells residing within the dCLNs, where MBP regulatory self-peptides were found on MHC-II molecules, but we did not find these MBP-specific CD4⁺ T cells in the sCLNs nor in the iLNs (Fig. 2l). A substantial number of these

Fig. 2 | MBP is non-encephalitogenic and fosters immunosuppression.

a, EAE was assessed in C57BL/6J mice immunized with MOG_{35–55} or MBP_{160–175}. $n = 5$ per group. Data are mean \pm s.e.m., representative of two independent experiments. Statistical analysis was performed using two-way analysis of variance (ANOVA). **b,c**, Draining iLNs were extracted from mice immunized with MOG_{35–55} or MBP_{160–175} on day 7. $n = 3$ per group. **b**, Quantification of cell counts. Data are mean \pm s.e.m. Statistical analysis was performed using unpaired two-tailed Student's *t*-tests. **c**, ELISpot assay of IL-2 production by CD4⁺T cells after recall with the indicated peptides. Data are mean \pm s.e.m. Statistical analysis was performed using two-way ANOVA with Šídák's post hoc test. Ag, antigen. **d**, EAE was evaluated for C57BL/6J male mice that were immunized with MOG_{35–55}, MOG_{35–55} + MBP_{160–175}(cit) or MOG_{35–55} + MBP_{160–175}. $n = 5$ per group. Data are mean \pm s.e.m., representative of three independent experiments. Statistical analysis was performed using two-way ANOVA with Dunnett's post hoc test. **e,f**, scRNA-seq analysis of T cells isolated from the draining iLNs of C57BL/6J mice immunized with MOG_{35–55} or MOG_{35–55} + MBP_{160–175} displayed as a UMAP projection (**e**) and the log₂-transformed fold change (**f**) of different T cell clusters; significant differences are indicated. $n = 3$ per group. T_{FH}, T follicular helper cells. For **f**, data are mean \pm s.e.m. **g**, Upregulated GO terms for CD4⁺ or CD8⁺T cells in the MOG_{35–55} + MBP_{160–175} versus MOG_{35–55}

group. Statistical analysis was performed using an over-representation test; *P* values were adjusted using the Benjamini–Hochberg method.

h,i, Representative flow cytometry plots (**h**) and quantification (**i**) of the proportion of CTLA-4⁺FOXP3⁺ or FOXP3⁺T_{reg} cells of CD4⁺T cells in the dCLN13 days after immunization. $n = 3$ per group. Data are mean \pm s.e.m. Statistical analysis was performed using unpaired two-tailed Student's *t*-tests. **j,k**, Representative flow cytometry plots (**j**) and quantification (**k**) of the proportion of CTLA-4⁺FOXP3⁺CD39⁺ cells of CD4⁺T cells in the spinal cord 13 days after immunization. $n = 5$ per group. Data are mean \pm s.e.m. Statistical analysis was performed using unpaired two-tailed Student's *t*-tests. **l**, Schematic of MBP-specific tetramer staining of CD4⁺T cells from dCLNs, sCLNs and iLNs of naive C57BL/6J mice; positive staining for MBP-specific CD4⁺T cells in the dCLN identifies FOXP3⁺ and CTLA-4⁺FOXP3⁺CD4⁺T cells. The diagram was created with BioRender.com. **m,n**, EAE was tracked in C57BL/6J male mice that were immunized with MOG_{35–55} or MOG_{35–55} + MBP_{160–175}. On days 7 and 10, the mice were treated with the following control or neutralizing antibodies: anti-CTLA-4 (**m**) or anti-TGF β (**n**). $n = 8$ (anti-CTLA-4 or IgG, MOG_{35–55} + MBP_{160–175}), $n = 6$ (anti-CTLA-4 MOG_{35–55}) and $n = 5$ per group (other groups). Data are mean \pm s.e.m., representative of three independent experiments. Statistical analysis was performed using two-way ANOVA with Dunnett's post hoc test. NS, not significant.

endogenous MBP-specific CD4⁺T cells presented the CTLA-4⁺FOXP3⁺ phenotype that we had previously noted to expand within the CNS at the onset of EAE with MBP_{160–175} co-immunization (Fig. 2*l*).

Given the well described function of CTLA-4 and TGF β as immunosuppressive molecules^{31,32}, we tested their role in supporting the suppressive properties of MBP immunization in fending against EAE. Indeed, compared with the isotype controls, neutralizing antibodies against either CTLA-4 or TGF β blunted the ability of MBP peptides to attenuate CNS autoimmunity (Fig. 2*m,n*). To investigate whether MBP-specific CD4⁺T cells directly use CTLA-4 and TGF β in the mechanism to restrain CNS autoimmunity, we further used MHC-II tetramers to study them *in vitro*. Compared with tetramer-negative polyclonal CD4⁺T cells, MBP-specific CD4⁺T cells significantly reduced the effector output of MOG-specific CD4⁺T cells, and this also depended on both CTLA-4 and TGF β (Extended Data Fig. 6*h,i*). Furthermore, concordant with its regulatory phenotype, we found that neutralizing antibodies against IL-10 also attenuated MBP-mediated suppression of EAE (Extended Data Fig. 6*j*). Bearing in mind the contrast between the inflammatory character of MOG-specific T cells and the more suppressive phenotype of MBP-specific T cells, we sought to understand their differences, if any, in thymic selection. By using MHC-II tetramers to identify either MOG- or MBP-specific CD4⁺T cells, we found that MBP-specific CD4⁺T cells exhibited a greater precursor frequency in the thymus of one-month-old C57BL/6J mice in comparison to MOG-specific CD4⁺T cells (Extended Data Fig. 6*k–m*). Consistent with central tolerance mechanisms, this evidences greater selection pressures against self-reactive T cells, like those against MOG_{35–55}, that possess a propensity to acquire an effector phenotype. Thus, collectively, we demonstrate that MBP regulatory self-peptides (guardian peptides) reinforce suppressor CD4⁺T cells, using both CTLA-4 and TGF β to guard against CNS autoimmune disease.

Therapeutic use of guardian peptides

To assess whether the presentation of MBP peptides is altered during neuroinflammation, we collected the brain, dura and spinal cord from C57BL/6J male mice at the peak of EAE (day 16) to establish the MHC-II peptidome during pathology (Fig. 3*a*). MHC-II expression was found to be appreciably increased with neuroinflammation, thereby permitting adequate recovery of MHC-II-bound peptides using fewer mice (Extended Data Fig. 7*a,b*). When we compared the immunopeptidomes of EAE-induced and naive C57BL/6J mice, an obvious shift was observed in the repertoire of autoantigens presented on MHC-II molecules (Fig. 3*b*); MHC-II-bound peptides derived from apolipoprotein

E (APOE) and prostaglandin D2 synthase (PTGDS), among others, were consistently found to be elevated in both the brain and the dura of EAE mice relative to the naive controls. Notably, with neuroinflammatory disease, the presentation of peptides within the MBP_{158–195} region was found to be substantially diminished in both the brain and the dura, but this was not the case for the downstream MBP_{196–236} antigenic region (Fig. 3*b,c*). In fact, the only MBP-derived peptides that could be identified in either the brain or the spinal cord of EAE mice were those encompassing the MBP_{196–236} region (Extended Data Fig. 7*c*).

To understand the potential causes of this loss of MBP_{158–195} presentation on MHC-II molecules, we first tested whether different APCs possessed differential abilities to present MBP peptides. As such, we began by enriching for different professional APCs, including CD11b⁺ macrophages, CD11c⁺ dendritic cells and CD19⁺B cells (Extended Data Fig. 7*d*). We then treated the cells with spinal cord homogenate, a mixture of CNS antigens, and performed immunopeptidomics to evaluate the collection of MBP peptides that could be identified on MHC-II molecules (Extended Data Fig. 7*d*). Both CD11b⁺ macrophages and CD11c⁺ dendritic cells exhibited the ability to present peptides within the MBP_{158–195} and MBP_{196–236} regions, whereas CD19⁺B cells could present peptides only within the MBP_{196–236} segment (Extended Data Fig. 7*e*). Moreover, when providing spinal cord homogenate to an I-A^b-expressing B cell line, it similarly revealed MHC-II-bound peptides solely contained within the MBP_{196–236} region (Extended Data Fig. 7*e*). Consistent with these results, when we used *Cx3cr1creERT2::MHC-IIfl/fl* mice to conditionally ablate MHC-II expression on parenchymal border macrophages³³ and collected the dural meninges for immunopeptidomics, we found that this diminished the relative abundance of MBP_{158–195} peptides bound to MHC-II (Extended Data Fig. 7*f–h*). Thus, these observations suggest that differences between the professional APCs of the myeloid and lymphoid lineages influence their ability to present regulatory MBP peptides.

We next considered inflammation-induced alterations in antigen processing and their potential impact on the presentation of regulatory MBP peptides. By comparing the C termini of MHC-II-bound peptides across EAE and naive mice, we observed obvious changes to the cleavage profile—EAE-induced mice had a significantly decreased predilection for basic residues at the C terminus relative to naive mice (Extended Data Fig. 8*a*). Knowing that myeloid cells in the CNS are major contributory APCs to both the initiation and progression of neuroinflammatory disease, we used a publicly available scRNA-seq dataset³³ to understand alterations to their antigen-processing machinery in the context of EAE. While the vast majority of microglia lacked MHC-II expression in homeostasis, neuroinflammation induced a

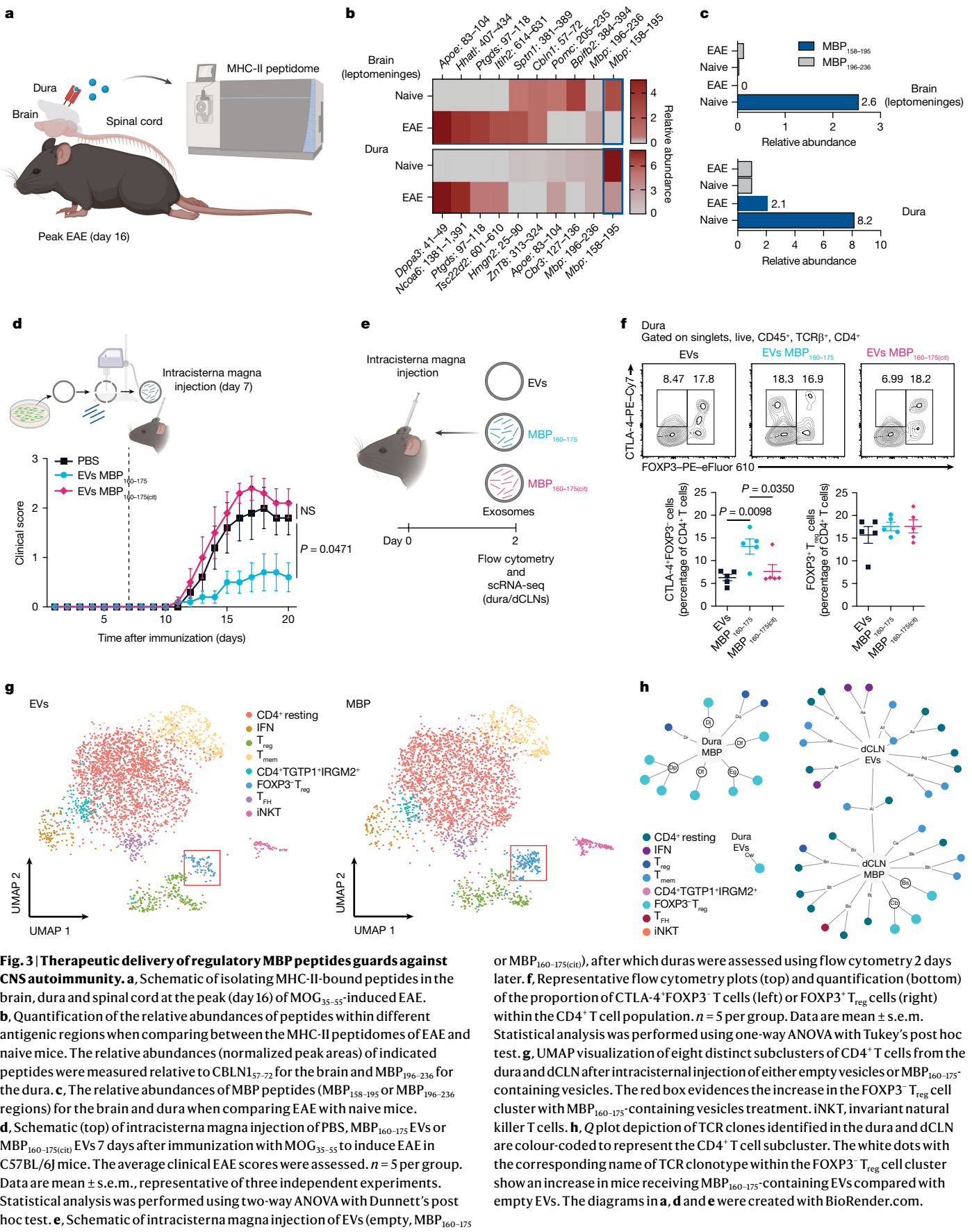


Fig. 3 | Therapeutic delivery of regulatory MBP peptides guards against CNS autoimmunity. **a**, Schematic of isolating MHC-II-bound peptides in the brain, dura and spinal cord at the peak (day 16) of MOG_{35–55}-induced EAE. **b**, Quantification of the relative abundances of peptides within different antigenic regions when comparing between the MHC-II peptidomes of EAE and naive mice. The relative abundances (normalized peak areas) of indicated peptides were measured relative to CBLN1_{57–72} for the brain and MBP_{196–236} for the dura. **c**, The relative abundances of MBP peptides (MBP_{158–195} or MBP_{196–236} regions) for the brain and dura when comparing EAE with naive mice. **d**, Schematic (top) of intracisterna magna injection of PBS, MBP_{160–175} EVs or MBP_{160–175(cit)} EVs 7 days after immunization with MOG_{35–55} to induce EAE in C57BL/6J mice. The average clinical EAE scores were assessed. $n = 5$ per group. Data are mean \pm s.e.m., representative of three independent experiments. Statistical analysis was performed using two-way ANOVA with Dunnett's post hoc test. **e**, Schematic of intracisterna magna injection of EVs (empty, MBP_{160–175}

or MBP_{160–175(cit)}), after which duras were assessed using flow cytometry 2 days later. **f**, Representative flow cytometry plots (top) and quantification (bottom) of the proportion of CTLA-4⁺FOXP3⁺ T cells (left) or FOXP3⁺T_{reg} cells (right) within the CD4⁺ T cell population. $n = 5$ per group. Data are mean \pm s.e.m. Statistical analysis was performed using one-way ANOVA with Tukey's post hoc test. **g**, UMAP visualization of eight distinct subclusters of CD4⁺ T cells from the dura and dCLN after intracisternal injection of either empty vesicles or MBP_{160–175}-containing vesicles. The red box evidences the increase in the FOXP3⁺T_{reg} cell cluster with MBP_{160–175}-containing vesicles treatment. iNKT, invariant natural killer T cells. **h**, Q plot depiction of TCR clones identified in the dura and dCLN are colour-coded to represent the CD4⁺ T cell subcluster. The white dots with the corresponding name of TCR clone type within the FOXP3⁺T_{reg} cell cluster show an increase in mice receiving MBP_{160–175}-containing EVs compared with empty EVs. The diagrams in **a**, **d** and **e** were created with BioRender.com.

Article

disease-associated microglial phenotype with a marked enhancement in MHC-II expression and genes involved in antigen processing and presentation³⁴ (Extended Data Fig. 8b,d). Indeed, we found that, at the peak of EAE disease, there was increased expression of peptidases, including cathepsins and caspases, among others (Extended Data Fig. 8c). Moreover, by treating bone-marrow-derived myeloid cells with lipopolysaccharide (LPS), an inflammatory trigger, before providing spinal cord homogenate and isolating MHC-II-bound peptides, we observed a complete absence of the presentation of the MBP_{158–195} region; this was not the case for the MBP_{196–236} region, as it still retained some capacity to be presented on MHC-II molecules and the presentation of other CNS-derived peptides remained unchanged (Extended Data Fig. 8e–g). Together, these data show that the intrinsic nature of the professional APCs and context-dependent alteration of antigen processing mechanisms affect the capacity for regulatory MBP peptides to be bound to MHC-II molecules.

The abundance of MBP_{158–195} presentation on MHC-II molecules during homeostasis and its curtailment with acute neuroinflammation led us to use these endogenous regulatory MBP peptides to ameliorate CNS autoimmunity. By taking advantage of advancements in the therapeutic use of extracellular vesicles (EVs) and a recent demonstration of its ability to modulate EAE disease^{35,36}, we encapsulated MBP_{160–175} peptides within EVs to test their efficacy as a potential antigen-specific immunotherapy (Extended Data Fig. 9a and Supplementary Fig. 1). Furthermore, given that MBP-specific CD4⁺ T cells reside endogenously in the CNS during homeostasis, we wondered whether this would suffice to defend against CNS autoimmune disease. Congruous with our expectation, in EAE-induced mice that had received EVs containing MBP_{160–175} peptides before the onset of EAE symptoms, CNS autoimmunity was significantly suppressed in comparison to in control mice receiving EVs with MBP_{160–175(cit)}, EVs with MBP_{192–216} or EVs with OVA_{323–339} (Fig. 3d and Extended Data Fig. 9b). Furthermore, EV-mediated delivery of MBP_{160–175} was necessary for its protection, as intracisternal injection of unencapsulated MBP_{160–175} peptides did not alter disease progression (Extended Data Fig. 9c).

Notably, introduction of EVs containing MBP_{160–175} into the cerebrospinal fluid (CSF) resulted in an expansion in the CTLA-4⁺FOXP3⁺CD4⁺ suppressor T cells that we had observed earlier in the dura (Fig. 3e,f). Injection of empty EVs or of EVs with MBP_{160–175(cit)} did not upregulate this CTLA-4⁺FOXP3⁺CD4⁺ suppressor T cell population (Fig. 3f) and, indeed, there were no differences in the frequencies of regulatory FOXP3⁺CD4⁺ T cells across all of the tested conditions (Fig. 3f). Moreover, similar changes were consistently observed across multiple LNs, including the dCLNs and sCLNs, but the spleen was not affected (Extended Data Fig. 9d–g). To understand this further, we performed scRNA-seq analysis of the dura and the dCLNs after providing empty or MBP_{160–175}-containing vesicles directly into the CSF. Consistent with flow cytometry data, we noted a distinct and significant increase in the unconventional FOXP3⁺ regulatory T (T_{reg}) cell cluster but not in the conventional FOXP3⁺T_{reg} cells (Fig. 3g and Extended Data Fig. 10a–c). Moreover, clonal expansion to both the FOXP3⁺ and FOXP3[−]T_{reg} clusters could be observed in the dura of mice that received MBP_{160–175}-containing vesicles (Fig. 3h and Extended Data Fig. 10d,e). Further, the FOXP3[−]T_{reg} cell cluster evidenced a suppressive transcriptional profile (for example *Ctla4*, *Tgfb1*, *Ptpn6*, *Ptpn11*), reiterating the functional importance of both CTLA-4 and TGFβ in MBP-mediated protection against CNS autoimmunity. Thus, collectively, we show that, by supplying the CSF with endogenous regulatory MBP peptides, we specifically boost the presence of MBP-specific suppressor CD4⁺ T cells and that this provides sufficient protection to the CNS against autoreactivity.

Discussion

Here we established the MHC-II peptidome of the CNS during homeostasis and identified endogenous self-peptides presented

predominantly along the brain's borders and within its draining LNs. These guardian self-peptides guided the immune response towards suppression and specifically boosted a population of unconventional suppressor FOXP3⁺CD4⁺ T cells. Notably, neuroinflammation resulted in loss of the presentation of endogenous regulatory self-peptides, and supplementation of the CSF with these peptides significantly ameliorated CNS autoimmune disease. This raises the possibility that the CNS seeks engagement of the adaptive immune system to acquire immune privilege. Moreover, we mainly focused on MBP peptides in this study, but it is foreseeable that this is simply one example of many other self-peptides that exhibit similar responses. Understanding their shared properties may prove to be advantageous for the development of antigen-specific therapies.

Furthermore, we demonstrated the direct binding of endogenous peptides sourced from the CNS to MHC-II molecules during homeostasis. We further highlight an increased prevalence of MHC-II-bound MBP peptides pervading the meningeal lymphatic network, extending from the brain parenchyma to the draining CLNs. Studies in other systems have indeed demonstrated that tissue-specific antigens are presented on MHC-II molecules during homeostasis in their respective draining LNs for the skin and intestines³⁷ as well as the pancreas³⁸. Thus, we provide evidence to further support the intentional need for an organ system to provide an 'image' of itself to calibrate the immune system towards self-tolerance³⁹.

These snapshots of self may very well be relayed to autoreactive CD4⁺ T cells through their presentation on MHC-II molecules. Strong support for this presumption comes from the present observation that our identified endogenous regulatory peptides reinforce a specific population of unconventional suppressor CD4⁺ T cells in the CNS, thereby spurring on the immune response toward suppression. Thus, we propose that the CNS may have evolved a parallel mechanism that enables its manipulation of the adaptive immune system to ensure CNS immune privilege, thereby adding an extra layer of protection to the physical barriers fortifying the CNS. A phenomenon of guardian autoimmunity presented here may apply to all other organs, particularly to ones with immune privilege, such as the eye and the reproductive organs.

During infection, to effectively mount an immune response against peripheral insults, the tissue shifts its focus to provide an image of the insult on MHC-II molecules to appropriately tailor the adaptive immune response. Effectively, the immune response evolved to necessitate, on occasion, the displacement of self-antigens presented during homeostasis to resolve the more pressing issue, inflammation. This introduces vulnerabilities to the system—while the immune response targets the insult, potential opportunities for pathologic self-reactivity through molecular mimicry arise^{40–42}. Here we demonstrate that both the intrinsic antigen-presenting qualities of different professional APCs and the inflammation-induced changes to antigen-processing capacities affect the presentation of regulatory self-peptides, like those contained within the MBP_{158–195} region. Both of these probably have a role in the shift observed in the MHC-II peptidome of the CNS and its borders during neuroinflammatory disease. Furthermore, our findings suggest that B cells do not appreciably present regulatory MBP peptides. This is interesting, as MS has been strongly associated with Epstein–Barr virus infection that infects and remains latent within B cells⁴³. Thus, on top of recent reports on cross-reactivity between Epstein–Barr virus and CNS-specific autoantigens^{42,44}, it is also foreseeable, in light of our study, that infiltrating B cells into the CNS shape the repertoire of MHC-II-bound endogenous peptides. This may contribute to the diminished presentation of regulatory self-peptides, like those contained within MBP_{158–195}, and promote the pathogenesis of CNS autoimmunity.

Our findings shed light on the aetiology of multiple sclerosis and of other autoimmune diseases in which peripheral infections alter the presentation of regulatory self-peptides and thereby expose the tissue to autoreactive attack. Furthermore, our study emphasizes an

attractive route along which these regulatory self-peptides can be therapeutically administered as an antigen-specific immunotherapy for autoimmune disorders. In summary, we demonstrate that the CNS purposefully presents itself on MHC-II molecules at the CNS borders (meninges) and that such presentation is critically important for its maintenance of immune tolerance.

Online content

Any methods, additional references, Nature Portfolio reporting summaries, source data, extended data, supplementary information, acknowledgements, peer review information; details of author contributions and competing interests; and statements of data and code availability are available at <https://doi.org/10.1038/s41586-024-08279-y>.

1. Rustenhoven, J. & Kipnis, J. Brain borders at the central stage of neuroimmunology. *Nature* **612**, 417–429 (2022).
2. Smyth, L. C. D. et al. Identification of direct connections between the dura and the brain. *Nature* **627**, 165–173 (2024).
3. Shirai, Y. On the transplantation of the rat sarcoma in adult heterogenous animals. *Jap. Med. World* **1**, 14–15 (1921).
4. Murphy, J. B. & Sturm, E. Conditions determining the transplantability of tissues in the brain. *J. Exp. Med.* **38**, 183–197 (1923).
5. Medawar, P. B. Immunity to homologous grafted skin; the fate of skin homografts transplanted to the brain, to subcutaneous tissue, and to the anterior chamber of the eye. *Br. J. Exp. Pathol.* **29**, 58–69 (1948).
6. Rustenhoven, J. & Kipnis, J. Bypassing the blood-brain barrier. *Science* **366**, 1448–1449 (2019).
7. Louveau, A. et al. Structural and functional features of central nervous system lymphatic vessels. *Nature* **523**, 337–341 (2015).
8. Absinta, M. et al. Human and nonhuman primate meninges harbor lymphatic vessels that can be visualized noninvasively by MRI. *eLife* **6**, e29738 (2017).
9. Rustenhoven, J. et al. Functional characterization of the dural sinuses as a neuroimmune interface. *Cell* **184**, 1000–1016 (2021).
10. Castellani, G., Croese, T., Peralta Ramos, J. M. & Schwartz, M. Transforming the understanding of brain immunity. *Science* **380**, eab07649 (2023).
11. Ota, K. et al. T-cell recognition of an immunodominant myelin basic protein epitope in multiple sclerosis. *Nature* **346**, 183–187 (1990).
12. Kipnis, J., Gadani, S. & Derecki, N. C. Pro-cognitive properties of T cells. *Nat. Rev. Immunol.* **12**, 663–669 (2012).
13. Schwartz, M. & Raposo, C. Protective autoimmunity: a unifying model for the immune network involved in CNS repair. *Neuroscientist* **20**, 343–358 (2014).
14. Richards, D. M., Kyewski, B. & Feuerer, M. Re-examining the nature and function of self-reactive T cells. *Trends Immunol.* **37**, 114–125 (2016).
15. Alspach, E. et al. MHC-II neoantigens shape tumour immunity and response to immunotherapy. *Nature* **574**, 696–701 (2019).
16. Reynisson, B. et al. Improved prediction of MHC II antigen presentation through integration and motif deconvolution of mass spectrometry MHC eluted ligand data. *J. Proteome Res.* **19**, 2304–2315 (2020).
17. Shao, X. M. et al. High-throughput prediction of MHC class I and II neoantigens with MHCnuggets. *Cancer Immunol. Res.* **8**, 396–408 (2020).
18. Sjöstedt, E. et al. An atlas of the protein-coding genes in the human, pig, and mouse brain. *Science* **367**, eaay5947 (2020).
19. Cserr, H. F., Harling-Berg, C. J. & Knopf, P. M. Drainage of brain extracellular fluid into blood and deep cervical lymph and its immunological significance. *Brain Pathol.* **2**, 269–276 (1992).
20. Louveau, A. et al. CNS lymphatic drainage and neuroinflammation are regulated by meningeal lymphatic vasculature. *Nat. Neurosci.* **21**, 1380–1391 (2018).
21. Mendel, I., Kerlero de Rosbo, N. & Ben-Nun, A. A myelin oligodendrocyte glycoprotein peptide induces typical chronic experimental autoimmune encephalomyelitis in H-2^b mice: fine specificity and T cell receptor V β expression of encephalitogenic T cells. *Eur. J. Immunol.* **25**, 1951–1959 (1995).
22. Weiner, H. L. The challenge of multiple sclerosis: how do we cure a chronic heterogeneous disease? *Ann. Neurol.* **65**, 239–248 (2009).
23. Steinman, L. Immunology of relapse and remission in multiple sclerosis. *Annu. Rev. Immunol.* **32**, 257–281 (2014).
24. Bernard, C. C. Experimental autoimmune encephalomyelitis in mice: genetic control of susceptibility. *J. Immunogenet.* **3**, 263–274 (1976).
25. Valesini, G. et al. Citrullination and autoimmunity. *Autoimmun. Rev.* **14**, 490–497 (2015).
26. Sospedra, M. & Martin, R. Immunology of multiple sclerosis. *Annu. Rev. Immunol.* **23**, 683–747 (2005).
27. Balashov, K. E., Rottman, J. B., Weiner, H. L. & Hancock, W. W. CCR5⁺ and CXCR3⁺ T cells are increased in multiple sclerosis and their ligands MIP-1 α and IP-10 are expressed in demyelinating brain lesions. *Proc. Natl. Acad. Sci. USA* **96**, 6873–6878 (1999).
28. Mackay, C. R. CXCR3⁺CCR5⁺ T cells and autoimmune diseases: guilty as charged? *J. Clin. Invest.* **124**, 3682–3684 (2014).
29. Dominguez-Villar, M. & Hafler, D. A. Regulatory T cells in autoimmune disease. *Nat. Immunol.* **19**, 665–673 (2018).
30. Antonioli, L., Pacher, P., Vizi, E. S. & Hasko, G. CD39 and CD73 in immunity and inflammation. *Trends Mol. Med.* **19**, 355–367 (2013).
31. Battle, E. & Massague, J. Transforming growth factor- β signaling in immunity and cancer. *Immunity* **50**, 924–940 (2019).
32. Walker, L. S. & Sansom, D. M. The emerging role of CTLA4 as a cell-extrinsic regulator of T cell responses. *Nat. Rev. Immunol.* **11**, 852–863 (2011).
33. Jordao, M. J. C. et al. Single-cell profiling identifies myeloid cell subsets with distinct fates during neuroinflammation. *Science* **363**, eaat7554 (2019).
34. Butovsky, O. & Weiner, H. L. Microglial signatures and their role in health and disease. *Nat. Rev. Neurosci.* **19**, 622–635 (2018).
35. Wiklander, O. P. B., Brennan, M. A., Lotvall, J., Breakfield, X. O. & El Andaloussi, S. Advances in therapeutic applications of extracellular vesicles. *Sci. Transl. Med.* **11**, eaav8521 (2019).
36. Casella, G. et al. Oligodendrocyte-derived extracellular vesicles as antigen-specific therapy for autoimmune neuroinflammation in mice. *Sci. Transl. Med.* **12**, eaba0599 (2020).
37. Fugmann, T., Sofroni, A., Ritz, D., Bootz, F. & Neri, D. The MHC class II immunopeptidome of lymph nodes in health and in chemically induced colitis. *J. Immunol.* **198**, 1357–1364 (2017).
38. Wan, X. et al. The MHC-II peptidome of pancreatic islets identifies key features of autoimmune peptides. *Nat. Immunol.* **21**, 455–463 (2020).
39. Cohen, I. R. The cognitive paradigm and the immunological homunculus. *Immunol. Today* **13**, 490–494 (1992).
40. Wucherpfennig, K. W. & Strominger, J. L. Molecular mimicry in T cell-mediated autoimmunity: viral peptides activate human T cell clones specific for myelin basic protein. *Cell* **80**, 695–705 (1995).
41. Lunemann, J. D. et al. EBNA1-specific T cells from patients with multiple sclerosis cross react with myelin antigens and co-produce IFN- γ and IL-2. *J. Exp. Med.* **205**, 1763–1773 (2008).
42. Lanz, T. V. et al. Clonally expanded B cells in multiple sclerosis bind EBV EBNA1 and GlialCAM. *Nature* **603**, 321–327 (2022).
43. Robinson, W. H. & Steinman, L. Epstein-Barr virus and multiple sclerosis. *Science* **375**, 264–265 (2022).
44. Thomas, O. G. et al. Cross-reactive EBNA1 immunity targets alpha-crystallin B and is associated with multiple sclerosis. *Sci. Adv.* **9**, eadg3032 (2023).

Publisher's note Springer Nature remains neutral with regard to jurisdictional claims in published maps and institutional affiliations.



Open Access This article is licensed under a Creative Commons Attribution-NonCommercial-NoDerivatives 4.0 International License, which permits any non-commercial use, sharing, distribution and reproduction in any medium or format, as long as you give appropriate credit to the original author(s) and the source, provide a link to the Creative Commons licence, and indicate if you modified the licensed material. You do not have permission under this licence to share adapted material derived from this article or parts of it. The images or other third party material in this article are included in the article's Creative Commons licence, unless indicated otherwise in a credit line to the material. If material is not included in the article's Creative Commons licence and your intended use is not permitted by statutory regulation or exceeds the permitted use, you will need to obtain permission directly from the copyright holder. To view a copy of this licence, visit <http://creativecommons.org/licenses/by-nc-nd/4.0/>.

© The Author(s) 2024

Article

Methods

Mice

C57BL/6J (WT; JAX000664) and SJL/J (WT; JAX000686) mice were purchased from the Jackson Laboratory. Transgenic mice (*Cx3cr1*^{creERT2} and *H2-Ab1*^{f/f}, gifted by K. Murphy) were maintained on a C57BL/6 background, and *Cx3cr1*^{creERT2} mice were crossed with *H2-Ab1*^{f/f} mice. All of the mice were maintained in standard housing conditions (temperature at 22 °C, humidity maintained between 33 and 39%, under a 12 h–12 h light–dark cycle, and provided with sterilized water and regular rodent chow ad libitum unless stated otherwise). Mice were allowed to acclimate for at least 1 week in the animal facility before the beginning of any experiment. Adult males and females between 8 and 12 weeks of age were primarily used for our studies unless stated otherwise. Sample sizes were determined on the basis of a power analysis in accordance with previously published experiments. Experimenters, where necessary, were blinded to experimental groups during both scoring and quantification. All of the experiments were approved by the Institutional Animal Care and Use Committee at the Washington University in St Louis.

Single-cell isolations

Brain (including leptomeninges), dural meninges, choroid plexus, spinal cord, LNs (that is, dCLNs, sCLNs and iLNs), thymus and spleen isolations were performed after lethal intraperitoneal (i.p.) injection of Euthasol. Subsequently, mice underwent transcardiac perfusion with PBS containing heparin (0.025%); the samples were collected into ice-cold Roswell Park Memorial Institute medium (RPMI, Gibco) and maintained on ice for the entirety of tissue collection. Spleens were removed from the surrounding tissues and placed onto ice-cold RPMI until further use. The whole spleen was digested and mashed through a 70 µm cell strainer with a glass pestle and washed with 5 ml of RPMI. Cells were then centrifuged at 450g for 5 min. Red blood cell lysis was performed with 1 ml of ammonium-chloride-potassium (ACK) lysis buffer (Quality Biological); cells were incubated for 2 min and then 2 ml of ice-cold PBS was supplemented to the sample. The samples were subsequently centrifuged at 450g for 5 min and lysed red blood cells were aspirated. The cell pellets were then resuspended in FACS buffer (2% BSA, 1 mM ethylenediaminetetraacetic acid (EDTA), 20 mM N-2-hydroxyethylpiperazine-N-2-ethane sulfonic acid (HEPES)) and kept on ice until further use. LNs and thymi were similarly digested and mashed through a 70 µm cell strainer, washed with 2 ml RPMI, centrifuged, resuspended in FACS buffer and kept on ice until further use. Choroid plexi were removed from the brain; similarly, the dural meninges were peeled from the skull cap using Dumont #5 forceps (Fine Science Tools). The dural meninges were kept in ice-cold RPMI for the entirety of tissue collection. Dural meninges were then digested for 15 min at 37 °C with constant agitation using 1 ml of prewarmed digestion buffer (RPMI medium with 2% fetal bovine serum (FBS, Gibco), 1 mg ml⁻¹ collagenase VIII (Sigma-Aldrich) and 0.5 mg ml⁻¹ DNase I (Thermo Scientific)). They were then filtered similarly through a 70 µm cell strainer and provided with 1 ml of complete medium (RPMI with 10% FBS) to neutralize the enzymes. The samples were then centrifuged at 450g for 5 min, resuspended in FACS buffer and kept on ice. Lastly, brains and spinal cords were collected and placed into ice-cold RPMI for the entirety of the collection. Brains were mechanically dissociated using sterile surgical scalpels into ~1 mm³ cubes and digested with constant agitation in 2 ml of prewarmed digestion buffer for 20 min at 37 °C, triturated with a 10 ml serological pipette, digested for another 20 min, triturated with a 5 ml serological pipette and digested for an additional 20 min. To remove myelin, a 1:1 ratio of 22% BSA in PBS was added and centrifuged at 1,000g for 10 min. After centrifugation, the floating myelin layer was aspirated. Cell pellets were then neutralized with RPMI with 10% FBS to halt the enzymatic digestion. An additional 5 ml of RPMI with 10% FBS was added to wash the pellet. The samples

were centrifuged at 450g for 5 min, resuspended in FACS buffer and kept on ice until use.

Flow cytometry

Single-cell suspensions were acquired as described above in the ‘Single-cell isolations’ section. Where MHC-II tetramer staining was performed, single-cell suspensions were first enriched for CD4⁺ T cells using EasySep Mouse CD4⁺ T cell isolation kit (StemCell Technologies). Beforehand, reagents were prepared by conjugating biotinylated MHC-II monomers (MBP, MOG, CLIP (control)) with streptavidin-PE and streptavidin-APC at 4 °C. Enriched CD4⁺ T cells were then incubated with respective MHC-II tetramers (MBP, MOG, CLIP (control)) at 37 °C for 20 min. Furthermore, they were supplemented with anti-PE beads (Miltenyi Biotec) and/or with anti-APC beads (Miltenyi Biotec) to stabilize the binding interaction. Although variable across different MHC-II tetramers, binding identified up to 20% of T cells exhibiting its respective specificity. Thereafter, single-cell suspensions or MHC-II tetramer stained CD4⁺ T cells were funnelled through similar staining protocols. They were incubated with Zombie NIR (BioLegend) diluted 1:800 in ice-cold PBS for 15 min at 4 °C for viability staining. The samples were then subsequently centrifuged, resuspended in FACS buffer containing anti-CD16/32 (Fc block; BioLegend) diluted 1:100 in FACS buffer for 5 min. Cells were then stained for 30 min at 4 °C for surface markers with antibodies diluted appropriately in FACS buffer; this was typically at 1:200 final concentration unless stated otherwise. For surface staining only, the samples were washed in FACS buffer and ran on the Aurora spectral flow cytometer (Cytek) then analysed using FlowJo (Tree Star). Data processing and statistical analysis were performed using GraphPad Prism. For samples requiring intracellular staining, surface staining was performed first as described above. Then, cells were fixed and permeabilized using the FOXP3/Transcription Factor Staining Buffer Set (eBioscience); staining was performed for 30 min at 4 °C with fluorescently conjugated antibodies against intracellular molecules. Antibodies were diluted 1:100 for intracellular staining. Similar to above, after staining, the samples were washed with FACS buffer and were run on the Aurora spectral flow cytometer. Data were analysed using FlowJo, after which the data were further processed and statistically analysed using GraphPad Prism. A full list of antibodies used is provided in Supplementary Table 2.

Isolation of the MHC-II peptidome

Tissues were collected from 110 8–10-week-old C57BL/6J male mice, 8–10-week-old C57BL/6J female mice and 8–10-week-old SJL/J male mice, as well as 20 8–10-week-old C57BL/6J male mice induced with EAE. Moreover, duras were collected from 20 8–10-week-old *Cx3cr1*^{creERT2}::MHC-II^{f/f} mice as well as 10 8–10-week-old *Cx3cr1*^{creERT2}::MHC-II^{t/+} mice 2 weeks after tamoxifen (treated daily at 100 mg per kg body weight for 3 consecutive days and assessed 2 weeks thereafter); differences in the number of mice used account for equitable isolation of MHC-II-expressing cells. Cells were isolated as described in the “Single-cell isolations” section.

For in vitro experiments with spinal cord homogenate, cells were cultured together with spinal cord homogenate for 6 h before further processing into single-cell suspensions. To assess the quality of CNS antigens presented on different APCs, spleens were collected from 8–10-week-old C57BL/6J mice. After single-cell isolations, CD11b⁺ macrophages were purified with CD11b MicroBeads UltraPure (Miltenyi Biotec), CD11c⁺ dendritic cells were enriched using CD11c MicroBeads UltraPure (Miltenyi Biotec) and CD19⁺ B cells were isolated using the EasySep Mouse B cell Isolation Kit (StemCell Technologies). M12.C3, a B cell lymphoma line, expressing I-A^b (gifted by X. Wan) maintained in culture with RPMI medium supplemented with 10% FBS (Gibco), 1% penicillin–streptomycin (Gibco), 2 mM L-glutamine (Gibco), and 50 µM β-mercaptoethanol (Thermo Fisher Scientific). For the generation of bone-marrow-derived myeloid cells, femurs were collected from 6–8-week-old C57BL/6J mice. They were subsequently flushed to isolate

bone marrow cells and maintained thereafter in a 100 mm culture dish with RPMI full medium, as detailed above, and also supplemented with murine granulocyte-macrophage colony-stimulating factor (GM-CSF, BioLegend). Then, 2–3 days later, half of the medium was removed and replaced with fresh RPMI medium containing GM-CSF. Cells were cultured for another 2–3 days to allow sufficient differentiation into myeloid cells. For experimentation, before supplementation with spinal cord homogenate, bone-marrow-derived myeloid cells were treated either with vehicle or LPS (Sigma-Aldrich) for 15 h.

All single-cell suspensions isolated as detailed above were then suspended in lysis buffer (40 mM MEGA 8, 40 mM MEGA 9, 1 mM phenylmethylsulfonyl fluoride, 0.2 mM iodoacetamide, 20 µg ml⁻¹ leupeptin and Roche cOmplete Protease Inhibitor cocktail in PBS) and rocked for 1 h at 4 °C. The cell lysate was centrifuged at 20,000g for 25 min at 4 °C. To remove peptides that non-specifically bind to Sepharose and/or immunoglobulin, the supernatant was first incubated with polyclonal mouse immunoglobulin G (IgG, Leinco Technologies; 1.5 mg antibody per sample) bound to Sepharose 4B at 4 °C for 30 min. The flow-through containing peptide–MHC-II complexes was collected, added to a tube containing PBS-washed Sepharose conjugated to the anti-I-A antibody (Y-3P; 1.5 mg per sample) and incubated at 4 °C overnight. The I-A-conjugated Sepharose was applied to a column and washed four times as follows: 10 ml 150 mM NaCl and 20 mM Tris (pH 7.4); 10 ml 400 mM NaCl and 20 mM Tris (pH 7.4); 10 ml 150 mM NaCl and 20 mM Tris (pH 7.4); and 10 ml 20 mM Tris (pH 8.0). Peptides were then eluted with 10% acetic acid and dried using the SpeedVac. Eluted peptides were passed over detergent-removal spin columns (Pierce) to remove traces of remaining detergent and were further cleaned using C18 Spin Columns from Thermo Fisher Scientific (Pierce).

MS analysis

A Dionex UltiMate 3000 system (Thermo Fisher Scientific) was coupled to an Orbitrap Fusion Lumos (Thermo Fisher Scientific) through an EASY-Spray ion source (Thermo Fisher Scientific). Before loading, peptide samples were reconstituted in 2% acetonitrile (ACN)/0.1% formic acid (17 µl). They were then subsequently loaded (15 µl, 15 µl min⁻¹; 3 min) onto a trap column (100 µm × 2 cm; 5 µm Acclaim PepMap 100 C18; 50 °C), eluted (0.2 µl min⁻¹) onto an EASY-Spray PepMap RSLC C18 column (2 µm; 50 cm × 75 µm inner diameter; 50 °C; Thermo Fisher Scientific) and separated with the following gradient (all percentage of buffer B, that is, 0.1% formic acid in acetonitrile): 0–110 min: 2–22% B; 110–120 min: 22–35% B; 120–130 min: 35–95% B; 130–150 min: isocratic at 95% B; 151–153 min: 95–2% B; 153–171 min: isocratic at 2% B. The spray voltage was 1,700 V, the ion-transfer tube temperature was 275 °C and the RF lens was 30%. MS scans were acquired in profile mode and tandem MS scans were acquired in centroid mode, for ions with charge states 2–7, with a cycle time of 1.5 s. MS spectra were recorded from 375–1,500 Da at 120,000 resolution (at *m/z* 200), and higher-energy collisional dissociation tandem MS was triggered above a threshold of 2.0×10^4 , with quadrupole isolation (1.4 Da) at 15,000 resolution and a collision energy of 30%. Dynamic exclusion was used (60 s), and monoisotopic precursor selection was on.

MS data analysis

Data files were uploaded to PEAKS Studio v.10.6 (Bioinformatics Solutions) for processing, de novo sequencing and database searching. The sequences were searched against the UniProt Mouse database (downloaded 4 January 2022; 22,102 entries) with mass error tolerances of 10 ppm and 0.02 Da for parent and fragment, respectively; no enzyme specificity; and oxidation (M), deamidation (NQ) and cysteine oxidation to cysteic acid as variable modifications. The Common Repository for Adventitious Proteins database (www.thegpm.org/crap/) was used to identify any contaminating proteins. False-discovery rate (FDR) estimation was enabled. Peptides were filtered at a 5% FDR or a $-\log_{10}[P]$ score of 15 (whichever was higher), and protein filtering was disabled

by setting the protein $-\log_{10}[P]$ score at 0 with one unique peptide and a requirement for significant peptides. For relative quantification of the different antigenic regions found in our peptidomes, we normalized peak areas to the total ion current, grouped overlapping peptide sequences into families and summed their peak areas, where relevant. We then picked a common peptide family sequence for which similar peak areas could be identified to allow for comparisons between peptidomes of interest. Relative abundances were determined relative to the above-stated common peptide family sequence.

EAE

EAE was induced in C57BL/6J mice by subcutaneous injection of MOG_{35–55} peptide (100 µg, CSBio) and/or different synthesized peptides at 100 µg each including, MBP_{160–175}, MBP_{160–175(cit)}, MBP_{166–185} or MBP_{192–216} (GenScript) emulsified in Freund's adjuvant (Sigma-Aldrich) supplemented with 2 mg ml⁻¹ of *Mycobacterium tuberculosis* (BD). Consistent with identification by MS, MBP_{160–175} was numbered based on golli-MBP; the sequence itself is conserved and corresponds to MBP_{27–42} of the classic MBP isoform. Pertussis toxin (200 ng, List Biologicals) was injected i.p. on day 0 and day 2 after immunization with MOG and/or MBP. EAE was induced in SJL/J mice by subcutaneous injection of PLP_{139–151} (100 µg, Vivitide) and/or different synthesized peptides at 100 µg each, including MBP_{160–175} or neurofilament light polypeptide (NEFL)_{160–173} (GenScript) emulsified in Freund's adjuvant (Sigma-Aldrich) supplemented with 2 mg ml⁻¹ of *M. tuberculosis* (BD). Pertussis toxin (400 ng, List Biologicals) was injected i.p. on day 0 and day 2 after immunization with PLP and/or MBP and NEFL. Where indicated, mice were injected i.p. with neutralizing antibodies against CTLA-4 (Bio X Cell; 250 µg per mouse), against IL-10 (Bio X Cell; 250 µg per mouse), or against TGFβ (Bio X Cell; 400 µg per mouse) at day 7 and 10 after immunization; matched dosing of IgG isotype antibodies were used as controls (Bio X Cell). For clinical evaluation, mice were scored daily: 0, no clinical disease; 1, limp tail; 2, hindlimb weakness; 3, hindlimb paralysis; 4, partial front limb paralysis; 5, moribund. A full list of the peptide sequences used is provided in Supplementary Table 3.

ELISpot analysis

Mice were subcutaneously immunized with different peptides, including MOG_{35–55}, MBP_{160–175}, MBP_{166–185} and MBP_{192–216}, among others, emulsified in Freund's adjuvant. 1 day before collection, 96-well polyvinylidene fluoride (PVDF) membrane plates (Millipore) were coated with IL-2 capture antibodies (BD Biosciences). 7 days after immunization, cells were isolated from the draining LNs and counted such that 5×10^5 cells would be loaded per well (each condition performed in triplicates). Cells were stimulated with their appropriate antigens and controls and incubated at 37 °C in 5% CO₂ for 24 h. IL-2-secreting cells were identified using IL-2 detection antibodies (BD Biosciences) and plates were developed according to the manufacturer's directions (BD Biosciences). Spots were quantified using CTL ImmunoSpot S6 Universal machines and Professional v.6.0.0 software.

scRNA-seq

iLN T cells. C57BL/6J male mice were immunized either with MOG_{35–55} or MOG_{35–55} along with MBP_{160–175} (*n* = 3 per group) and, 10 days later, cells from the draining (inguinal) LNs were collected. Cells were isolated as described in the 'Single-cell isolations' section and sorted to capture those negative for DAPI (live cells), Thy1.2 and TCRβ to capture both CD4⁺ and CD8⁺ T cells for single-cell sequencing. Sample loading and library construction were performed using the 10x Genomics Chromium platform and Chromium Single Cell 3' Library & Gel Bead Kit version 3 and libraries were sequenced on the Illumina NextSeq 500 system.

Reads were aligned to the mm10 genome using the Cellranger software pipeline provided by 10x genomics. The resulting filtered gene-by-cell matrices of unique molecular identifier (UMI) counts were read into R using the read10xCounts function from the Droplet Utils

Article

package. Cells were first filtered by manual removal of cells that had greater than 2.5 s.d. from the mean of either total RNA count or unique features in both directions, or 3 s.d. for the percentage of mitochondrial transcripts above the mean. Expression values for the final subset were then normalized using the scran and scater packages. The resulting log₂-transformed values were transformed to the natural-log scale for compatibility with the Seurat (v.3) pipeline^{45–47}.

The filtered and normalized matrix was used as input to the Seurat pipeline and cells were scaled across each gene, regressing out sequencing depth per cell, number of unique features and percentage mitochondrial reads, before the selection of the top 2,000 most highly variable genes using variance stabilizing transformation. Principal component analysis (PCA) was conducted and an elbow plot was used to select components for UMAP analysis and clustering. Shared nearest neighbour (SNN) clustering optimized with the Louvain algorithm, as implemented by the Seurat FindClusters function was performed before manual annotation of clusters based on expression of canonical gene markers. Initial contamination in the form of clusters with markers of B cells or myeloid lineage as well as doublets was manually removed and the finalized subset of cells was scaled, and underwent PCA, clustering and annotation as described above. Statistical analysis of cluster proportions was done using a permutation test with 1,000 instances followed by bootstrapping to produce a Pvalue and confidence interval.

For analysis of differentially expressed genes between conditions, CD4 and CD8 cells were subset based on subcluster identity and gene expression and each subset was filtered to include genes that had at least 4 transcripts in at least 4 cells. Then the top 2,000 highly variable genes were determined and included for further analysis using the SingleCellExperiment modelGeneVar and getTopHVGs functions. After filtering, limma and edgeR were used to build a model and conduct differential expression testing with the lmFit, contrasts.fit and eBayes functions. The results were then filtered using a Benjamini–Hochberg-adjusted P-value threshold of less than 0.05 as statistically significant. Over-representation enrichment analysis with Fisher's exact tests was used to determine significantly enriched GO terms ($P_{adj} < 0.05$) for the sets of significantly differentially expressed genes. For each gene set, genes were separated into up- and downregulated and separately⁴⁸ the enrichGO function from the clusterProfiler package was used with a gene set size set between 10 and 500 genes and Pvalues adjusted using Benjamini–Hochberg correction⁴⁹. Up- or downregulated peptidases were identified using the publicly available MEROPS database⁵⁰.

For differential gene expression analysis, the samples were grouped into naive, pre-symptomatic (includes pre-clinical 4 d and pre-clinical 8 d from original data analysis) and EAE (includes onset and acute from original data analysis). Microglia were subset and filtered to include genes that had at least 4 transcripts in at least 4 cells. The top 2,000 highly variable genes were then determined and included for further analysis using the SingleCellExperiment modelGeneVar and getTopHVGs functions. After filtering, limma and edgeR were used to build a model and conduct differential expression testing with the lmFit, contrasts.fit and eBayes functions. The results were then filtered using a Benjamini–Hochberg adjusted P-value threshold of less than 0.05 as statistically significant. Over-representation enrichment analysis with Fisher's exact test was used to determine significantly enriched GO terms ($P_{adj} < 0.05$) for the sets of significantly differentially expressed genes. For each gene set, genes were separated into up- and downregulated and separately⁴⁸ the enrichGO function from the clusterProfiler package was used with a gene set size set between 10 and 500 genes and Pvalues adjusted using Benjamini–Hochberg correction⁴⁹. Up- or downregulated peptidases were identified using the publicly available MEROPS database⁵⁰.

Dura, dCLN and tetramer isolated MBP-specific T cells. Empty EVs or MBP_{160–175}-containing EVs were introduced into C57BL/6J male mice through intracisterna magna injection ($n = 10$ per group). Then, 36 h later, cells from the dura as well as the CNS-draining dCLNs were collected as described in the 'Single-cell isolation' section. Single-cell suspensions were then sorted to capture cells negative for DAPI (live cells) and positive for Thy1.2 and TCRβ. Separately, C57BL/6J mice were immunized with MBP_{160–175} ($n = 8$ mice). Then, 1 week later, draining iLNs were collected as described in the 'Single-cell isolation' section. Cells were then stained with MHC-II tetramers as described in the 'Flow cytometry' section and sorted to capture cells negative for DAPI (live cells) and positive for Thy1.2 and TCRβ. Both MBP-tetramer-positive and MBP-tetramer-negative cells were sorted. Sample loading and library construction were performed using the 10x Genomics Chromium platform using the Chromium Single Cell 3v3.1 kit. Libraries were then sequenced on the Illumina NovaSeq 6000 system. Transcript-specific barcodes and sequencing libraries were constructed using the Chromium Single Cell 5' library and sequenced on the Illumina NovaSeq 6000 system.

Filtered gene-by-cell matrices of UMI counts from Cell Ranger v.7.2 for each sample were read into R using the Seurat Read10X function and converted into S4 objects using the CreateSeuratObject function. Quality-control filtering was applied to remove cells that expressed less than 1,200 unique genes as well as cells with over 15% mitochondrial gene expression. Cell Ranger's vdj workflow (v.6.1.1) was used for TCR data analysis. T cells with inappropriate combinations of α- and β-chains were removed.

Expression values were normalized and scaled across each gene using the NormalizeData and ScaleData functions from the Seurat v.4 package⁵¹. Sample datasets were then integrated with the Harmony package⁵². PCA was then conducted and the first 30 PCs were selected from an elbow plot for UMAP visualization. SNN clustering was optimized with the Louvain algorithm using the Seurat FindClusters function. The resulting clusters were then manually annotated based on canonical gene marker expression and then collapsed into the six clusters in the final dataset. Upregulated markers were generated using the Seurat FindMarkers function running a Wilcoxon rank-sum test and filtered to exclude any genes without a log₂-transformed fold change value < 0.25 , an adjusted Pvalue > 0.05 , as well as a min.pct factor < 0.1 . Significance statistics for cluster population proportions were calculated using the scProportionTest package⁵³. Clonal scatter plots, abundance plots and comparison plots were generated using the scRepertoire package⁵⁴.

Epitope prediction

To predict binding affinities of MHC-II-bound peptides for either C57BL/6J mice (I-A^b haplotype) or SJL/J (I-A^s haplotype) in the CNS and

Jordao EAE microglia analysis. CSV files containing single-cell transcript counts were downloaded from Gene Expression Omnibus accession GSE118948, read into R and converted to matrices. Blood and choroid plexus tissue samples were discarded and the remaining leptomeningeal and parenchymal perivascular space samples were manually filtered for quality control. Filtering was performed to remove cells with less than 200 unique genes, less than 1,000 or greater than 25,000 transcripts and a mitochondrial transcript percentage of greater than 30%. Expression values were then normalized using the scran and scater packages. The resulting log₂-transformed values were transformed to the natural-log scale for compatibility with the Seurat (v.3) pipeline^{45–47}. Initial contamination in the form of low-sequenced clusters was manually removed and the finalized subset of cells was scaled, and underwent PCA, clustering and annotation as described above.

The filtered and normalized matrix was used as input to the Seurat pipeline and cells were scaled across each gene, regressing out sequencing depth per cell, number of unique features and percentage of mitochondrial reads, before the selection of the top 2,000 most highly variable genes using variance stabilizing transformation. PCA was conducted and an elbow plot was used to select components for UMAP analysis and clustering. SNN clustering optimized with the Louvain algorithm, as implemented by the Seurat FindClusters function, was performed before manual annotation of clusters based on expression of canonical gene markers.

its associated tissues, we applied three independent models. These include an algorithm developed by us, using a hidden Markov model and trained on the most recent immune epitope database (IEDB)¹⁵ as well as publicly available platforms, such as netMHCIIpan-4.0¹⁶ and MHCnuggets¹⁷. As it is not possible to directly combine scores from different models, we calculated the percentile rank of the result score for each peptide and model against a large decoy set of random natural peptides. The mean (or median) value of percentiles across all models was then used as the main source for the given antigen. We further represented these values as inverted percentile ranks such that larger values indicate peptides with increased likelihood to be a binder. The decoy set was generated from the mouse proteome and consists of about 1×10^6 peptide fragments.

In vitro co-culture assays

For the generation of MOG- or MBP-specific hybridomas, C57BL/6 mice were immunized with MOG_{35–55} or MBP_{160–175}, respectively, into the flanks. Then, 1 week later, the draining iLNs were isolated and cultured in the presence of low-dose antigen (either MOG_{35–55} or MBP_{160–175} at 1 μ M). Then, 2–3 days later, lymphocytes were further separated using Histopaque-1119 (Sigma-Aldrich). Isolated lymphocytes were subsequently fused with BW5147.3 cells (T lymphoma line, gifted by X. Wan) with drop-wise addition of polyethylene glycol 1500 (Sigma-Aldrich). Dose-dependent curves to assay for antigen specificity were performed using IL-2 enzyme-linked immunosorbent assay (ELISA, Thermo Fisher Scientific) according to the manufacturer's protocol. To perform peptide competition assays to determine relative binding affinities, spleens were collected and processed as described in the 'Single cell isolations' section. CD11c⁺ dendritic cells were enriched using CD11c MicroBeads UltraPure (Miltenyi Biotech) and served as professional APCs. In 96-well flat bottom plates, CD11c⁺ dendritic cells were initially incubated at varying concentrations with competitor peptides (MBP_{160–175}, MBP_{160–175(cit)}, OVA_{323–339}) before the supplementation of the specific antigen (0.5 μ M MOG_{35–55}) for 1 h. Plates were centrifuged at 450g for 5 min and washed with full RPMI medium to rid of excess, unbound antigens. MOG-specific hybridomas, as generated above, were co-cultured with the CD11c⁺ dendritic cells pulsed with competitor peptide and MOG_{35–55}, its specific antigen, for 18–24 h. The supernatant was collected and was used to perform IL-2 ELISA (Thermo Fisher Scientific). For in vitro suppression assays, MOG- or MBP-specific primary T cells were isolated as follows. C57BL/6J mice were immunized with MOG_{35–55} or MBP_{160–175}, and the spleens and draining iLNs were collected 10 days later. Cells were isolated as described in the 'Single cell isolation' section. CD4⁺ T cells were enriched thereafter using EasySep Mouse CD4⁺ T cell isolation kit (StemCell Technologies). CD4⁺ T cells were then stained with MOG- or MBP-specific MHC-II tetramers conjugated to PE at 37 °C for 20 min and stabilized thereafter with anti-PE MicroBeads (Miltenyi Biotech). MOG- or MBP-specific CD4⁺ T cells were enriched by magnetic-activated cell sorting according to the manufacturer's protocol. From the enrichment of MBP-specific CD4⁺ T cells, the flow-through, containing tetramer-negative polyclonal CD4⁺ T cells, was retained as a control. Similarly to the above, CD11c⁺ dendritic cells isolated from spleens were used as professional APCs. They were cultured initially in 3 μ M MOG_{35–55} antigen for 1 h before being washed off with full RPMI medium. MOG-specific CD4⁺ T cells with either MBP-specific CD4⁺ T cells or tetramer-negative polyclonal CD4⁺ T cells were then added to the culture containing CD11c⁺ dendritic cells that had been pulsed with MOG_{35–55} antigen. IL-2 ELISA (Thermo Fisher Scientific) was performed according to the manufacturer's protocol to assay alterations to the reactivity of MOG-specific CD4⁺ T cells.

EV isolation and preparation

The DC2.4 cell line was purchased from the American Type Culture Collection (ATCC). Cells were maintained by culturing in Dulbecco's modified Eagle's medium (DMEM, Gibco) supplemented with 10% FBS

(Gibco), 1% penicillin-streptomycin (Gibco) and 2 mM L-glutamine (Gibco). All cells were grown in an incubator set at 37 °C in 5% CO₂. For the purposes of extracellular vesicle isolations, the DC2.4 cells were cultured in complete DMEM medium in T-75 flasks to 80–90% confluence. Cells were thoroughly washed with PBS before replacing the medium with serum-depleted DMEM. They were further cultured overnight. The supernatants were collected the next day and centrifuged at varying speeds, including at 1,000g for 10 min to rid of any cell contaminants as well as at 20,000g for 30 min to rid of any smaller debris. The supernatant was then further filtered with a 0.22 μ m filter and ultracentrifuged at 100,000g for 2 h to pellet down EVs. All centrifugations were performed at 4 °C. The pellet was resuspended in 500 μ l PBS and visualized by either transmission electron microscope (TEM, JEOL JEM-1400, Phillips) or nanoparticle tracking analysis (ZetaView) to confirm their isolation, to measure their size and to approximate the number of particles per ml (mean \pm s.d.). Isolated EVs were then sonicated with no antigen (empty EVs), MBP_{160–175}, MBP_{160–175(cit)}, MBP_{192–216} or OVA_{323–339} peptides at an amplitude equal to 20% for 6 cycles (30 s on, 2 min off). Next, the EVs were allowed to recover in the incubator set at 37 °C in 5% CO₂ for 1 h. To remove any unincorporated peptides and debris, we used the Exo-spin column according to the manufacturer's protocol (Cell Guidance Systems) to precipitate EVs of interest. Similarly to the above, EVs were assessed for successful purification by both TEM and nanoparticle tracking analysis. EVs were kept at –80 °C before intracisterna magna injection.

Western blotting

The supernatant or the pellet fraction after ultracentrifugation of EVs was resuspended in radio-immunoprecipitation assay (RIPA) buffer (Thermo Fisher Scientific). The samples were then appropriately diluted with 4 \times NuPAGE LDS sample buffer (Thermo Fisher Scientific) and boiled at 70 °C for 10 min. The samples were subsequently loaded onto 15-well SDS-PAGE precast gel (4–15% acrylamide gradient, Bio-Rad) and electrophoresis performed in Bio-Rad cassette. Gel electrophoresis ran at 100 V for 1 h, after which it was transferred to a methanol-activated PVDF membrane on ice for 2 h at 30 V. The membranes were then blocked with 5% (w/v) milk in Tris-buffered saline, 0.1% Tween-20 (TBS-T) for 1 h at room temperature. Primary antibodies, including anti-mouse CD9 (1:1,000, BioLegend) and anti-mouse CD63 (1:1,000, BioLegend), were diluted in 5% milk in TBS-T, after which they were used to stain the membrane overnight at 4 °C. The membranes were then washed three times with TBS-T. Appropriate secondary antibodies diluted 1:10,000 in 5% milk in TBS-T were used to stain the blot for 2 h at 4 °C. The membranes were washed again three times with TBS-T and developed thereafter using the Pierce ECL Western Blotting Substrate kit (Thermo Fisher Scientific). The blot was eventually imaged using the ChemiDoc MP gel imaging system (Bio-Rad).

Intracisterna magna injection

Mice were anaesthetized using ketamine–xylazine (100 mg per kg ketamine and 10 mg per kg xylazine). Their necks were shaved and cleaned appropriately with 70% iodine before placing their heads securely into the stereotactic frame. Ophthalmic solution was applied to prevent drying of their eyes before the procedure. Next, a longitudinal incision of the skin was made at the back of their necks; the underlying muscles were retracted with hooks to expose the cisterna magna. A 5 μ l Hamilton syringe with a 33-gauge needle was used to inject 5 μ l of PBS or EVs (that is, empty or containing MBP_{160–175}, MBP_{160–175(cit)}, MBP_{192–216} or OVA_{323–339}) at an approximate rate of 2.5 μ l min^{–1}, 10⁵ vesicles per μ l. To prevent backflow, the needle was not immediately retracted and kept within the cisterna magna for an additional minute after the injection. The skin was sutured, and the mice were maintained on a heating pad until fully awake. After the surgery, the mice received a subcutaneous injection of ketoprofen (2.5 mg per kg).

Statistical methods

Sample sizes, where necessary, were selected based on a standard power calculation ($\alpha = 0.05$, power of 0.8). Generally, statistical methods were not used to recalculate or to predetermine sample sizes. Variance was similar within comparable experimental groups. To ensure randomization, animals were selected from different cages but of the same experimental condition. Experimenters were kept blinded to the identity of groups before scoring up until data were collected and analysed. Statistical tests used for each figure, where necessary, were deemed appropriate. Unpaired *t*-tests were performed when comparing between two independent groups. One-way ANOVA with appropriate multiple-comparison tests was performed when comparing more than two independent groups. Two-way ANOVA with repeated-measures and appropriate multiple-comparison tests was performed when comparing three or more independent groups requiring clinical symptom evaluation with consistent observations. Statistical analysis was performed using GraphPad Prism. Data are always presented as mean \pm s.e.m.

Reporting summary

Further information on research design is available in the Nature Portfolio Reporting Summary linked to this article.

Data availability

Raw MS data and peptide-spectrum matches have been deposited in the MassIVE public proteomics repository (<http://massive.ucsd.edu>) under the identifier MSV000092643 and are available online (<ftp://massive.ucsd.edu/MSV000092643>). scRNA-seq data are available at the Gene Expression Omnibus under accession numbers GSE240691, GSE272901, GSE273051 and GSE276987.

Code availability

Custom code used in all scRNA-seq analyses is available from the authors on reasonable request.

45. Butler, A., Hoffman, P., Smibert, P., Papalexi, E. & Satija, R. Integrating single-cell transcriptomic data across different conditions, technologies, and species. *Nat. Biotechnol.* **36**, 411–420 (2018).
46. Lun, A. T., McCarthy, D. J. & Marioni, J. C. A step-by-step workflow for low-level analysis of single-cell RNA-seq data with Bioconductor. *F1000Res.* **5**, 2122 (2016).

47. McCarthy, D. J., Campbell, K. R., Lun, A. T. & Wills, Q. F. Scater: pre-processing, quality control, normalization and visualization of single-cell RNA-seq data in R. *Bioinformatics* **33**, 1179–1186 (2017).
48. Hong, G., Zhang, W., Li, H., Shen, X. & Guo, Z. Separate enrichment analysis of pathways for up- and downregulated genes. *J. R. Soc. Interface* **11**, 20130950 (2014).
49. Yu, G., Wang, L. G., Han, Y. & He, Q.-Y. clusterProfiler: an R package for comparing biological themes among gene clusters. *OMICS* **16**, 284–287 (2012).
50. Rawlings, N. D. et al. The MEROPS database of proteolytic enzymes, their substrates and inhibitors in 2017 and a comparison with peptidases in the PANTHER database. *Nucleic Acids Res.* **46**, D624–D632 (2018).
51. Hao, Y. et al. Integrated analysis of multimodal single-cell data. *Cell* **184**, 3573–3587 (2021).
52. Korsunsky, I. et al. Fast, sensitive and accurate integration of single-cell data with Harmony. *Nat. Methods* **16**, 1289–1296 (2019).
53. Miller, S. A. et al. LSD1 and aberrant DNA methylation mediate persistence of enteroendocrine progenitors that support BRAF-mutant colorectal cancer. *Cancer Res.* **81**, 3791–3805 (2021).
54. Borchering, N., Bormann, N. L. & Kraus, G. scRepertoire: an R-based toolkit for single-cell immune receptor analysis. *F1000Res.* **9**, 47 (2020).

Acknowledgements We thank S. Smith for her help in editing the manuscript; all of the members of the Kipnis laboratory for their continued discussions to push the current study forward; E. R. Unanue, X. Wan and A. N. Vomund for their insight and feedback in our efforts to establish the MHC-II peptidome of the CNS during physiology and pathology; the members of the Electron Microscopy Core within the Washington University Center for Cellular Imaging (WUCCI) for extracellular vesicle visualization; the members of the Flow cytometry and Fluorescence Activated Cell Sorting Core for sorting T cells for sequencing; the staff at the Genome Technology Access Center (GTAC) for performing the scRNA-seq; and the staff at the Bursky Center for Human Immunology and Immunotherapy at the Washington University in St Louis, particularly R. D. Schreiber and L. Yang, for their assistance in generating MHC-II tetramers. This work was supported by grants from the Barnes-Jewish Hospital investigators program and from the National Institutes of Health (DP1 AT010416) to J.K.

Author contributions M.W.K. conceptualized, designed and performed the experiments, analysed and interpreted the data, generated figures, and wrote and edited the manuscript. W.G. assisted in performing experiments and preparing samples for scRNA-seq. C.F.L. analysed samples using LC-MS/MS and performed database searches. X.G. assisted in performing experiments and preparing samples for scRNA-seq. T.D. performed scRNA-seq analyses and prepared the accompanying figures. J.C. performed scRNA-seq analyses and prepared the accompanying figures. I.S. performed any related animal surgeries. P.B. assisted in performing experiments. D.K. performed binding-affinity prediction analyses on the immunopeptidome datasets. A.F.M.S., A.D., K.K. and S.B. assisted in collecting tissues for MS. C.C., M.N.A. and E.R.U. provided intellectual contributions. J.K. conceptualized, provided resources, guided the analysis and interpretation of the generated data, and wrote and edited the manuscript.

Competing interests M.W.K. and J.K. hold provisional patent applications related to findings presented here.

Additional information

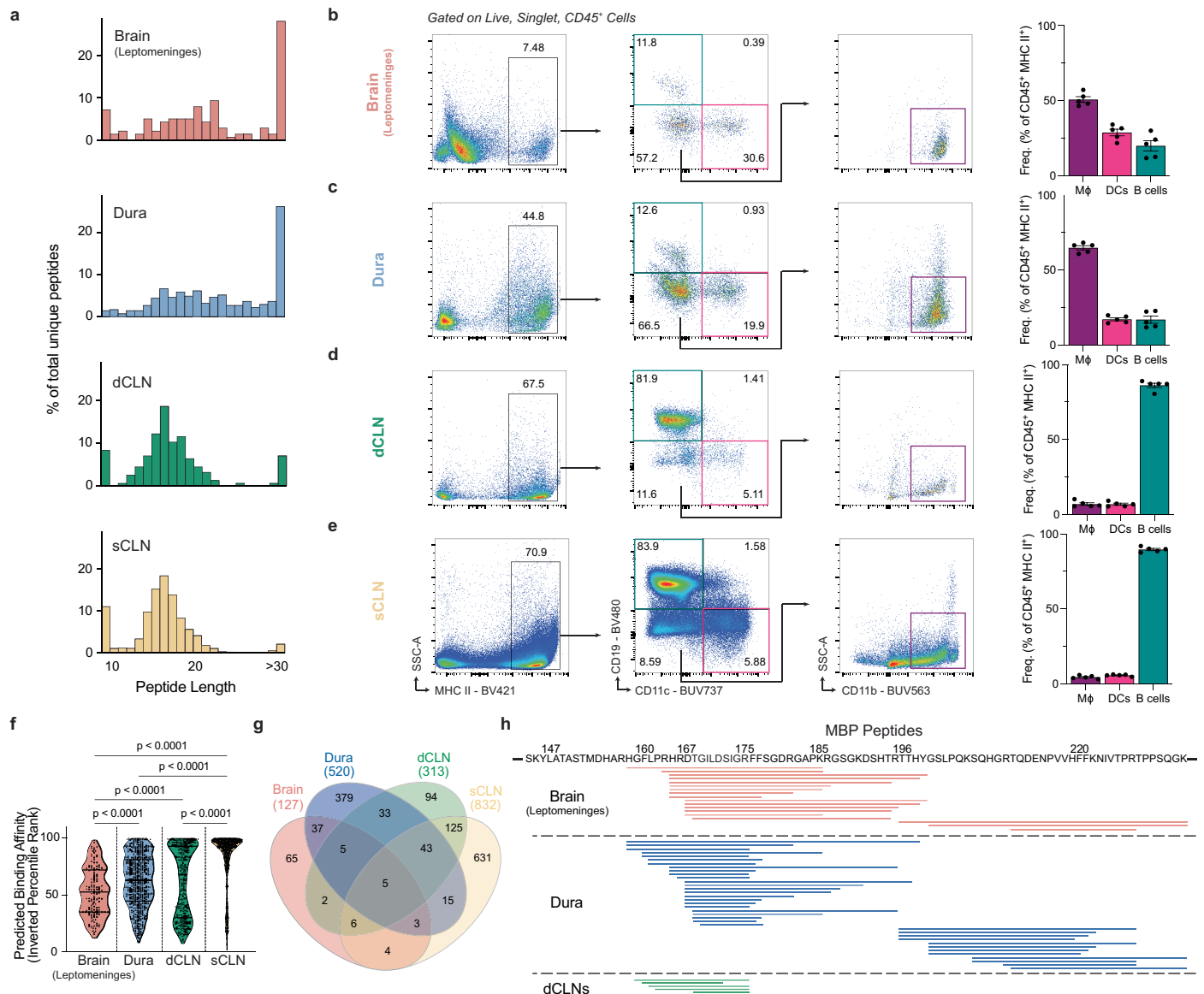
Supplementary information The online version contains supplementary material available at <https://doi.org/10.1038/s41586-024-08279-y>.

Correspondence and requests for materials should be addressed to Jonathan Kipnis.

Peer review information *Nature* thanks Vijay Kuchroo, Hartmut Wekerle and the other,

anonymous, reviewer(s) for their contribution to the peer review of this work.

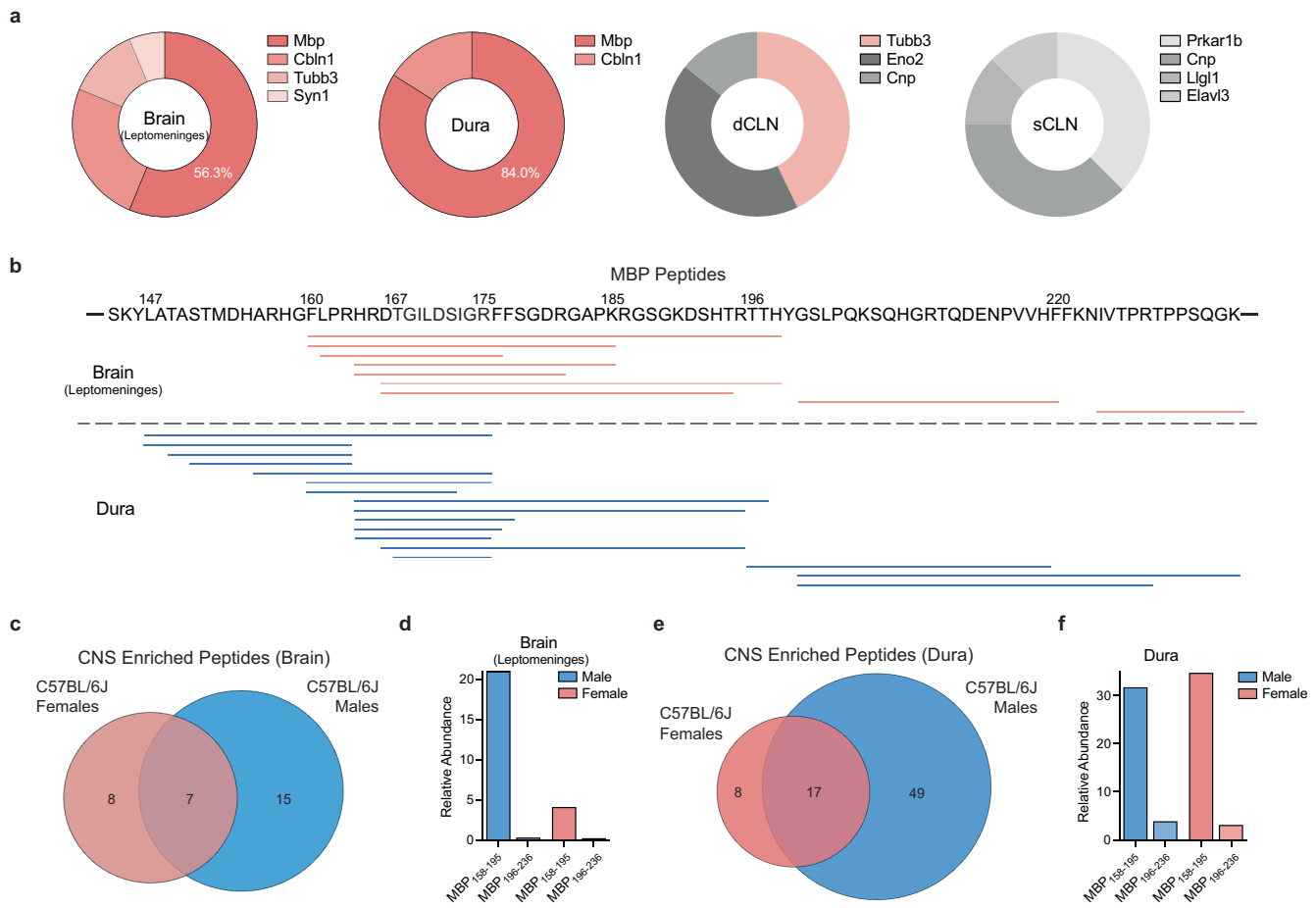
Reprints and permissions information is available at <http://www.nature.com/reprints>.



Extended Data Fig. 1 | Characterizing the CNS MHC II Peptidome of C57BL/6J male mice. **a**, Peptide length distribution represented as a percent of the total number of unique peptides identified by the MHC II peptidome for the brain (which also includes the leptomeninges), dura, dCLNs, and sCLNs. **b–e**, Representative flow cytometry plots depicting the gating strategy used to identify the distribution of MHC II-expressing cells. Within the MHC II⁺ gate, B cells (gated on CD19⁺ CD11c⁺), dendritic cells (DCs, gated on CD19⁻ CD11c⁺), and macrophages (MΦ, gated on CD19⁻ CD11c⁻ CD11b⁺) were identified. To the right, bar plots show the frequency of the aforementioned antigen presenting

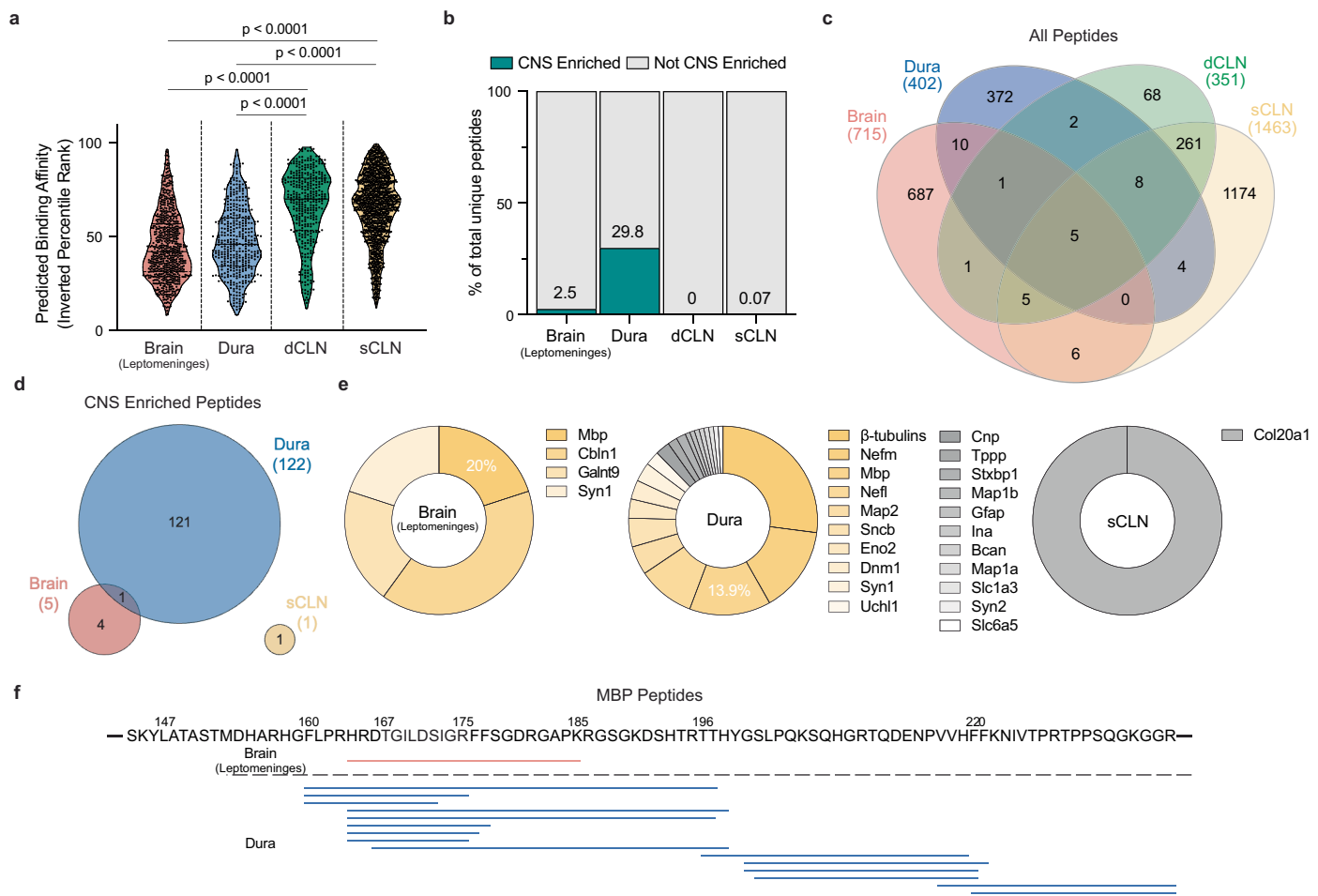
cells as a percent of CD45⁺ MHC II⁺ cells for the **(b)** brain, **(c)** dura, **(d)** dCLNs, and **(e)** sCLNs. (n = 5 mice analysed over 2 independent experiments; data shown as mean±s.e.m). **f**, Violin plot depicting predicted binding affinities for unique MHC II-bound peptides. The median is represented by a solid line and the first as well as the third quartiles are represented by dashed lines. P-values indicated on plot (one-way ANOVA with Tukey's multiple comparisons test). **g**, Venn diagram depicting the relationship between all unique MHC II-bound peptides in the brain, dura, dCLNs, and sCLNs. **h**, Summary of individual peptides identified on the MBP sequence as defined by the MHC II peptidome of C57BL/6J male mice.

Article



Extended Data Fig. 2 | The CNS MHC II peptidome of C57BL/6J female mice.
a, Pie chart defining the makeup of CNS-enriched, MHC II-bound peptides across each individual tissue. Percent of CNS-enriched peptides that are MBP are indicated in the plots, where relevant. **b**, Summary of all identified individual peptide sequences derived from MBP in the C57BL/6J female MHC II peptidome. **c**, Venn diagram representation of individual overlapping CNS-enriched peptide sequences identified between C57BL/6J females and males in the brain (including leptomeninges). **d**, Bar graph showing the relative abundance of MBP peptides in the brain that comprised either the MBP₁₅₈₋₁₉₅ or MBP₁₉₆₋₂₃₆ regions in both

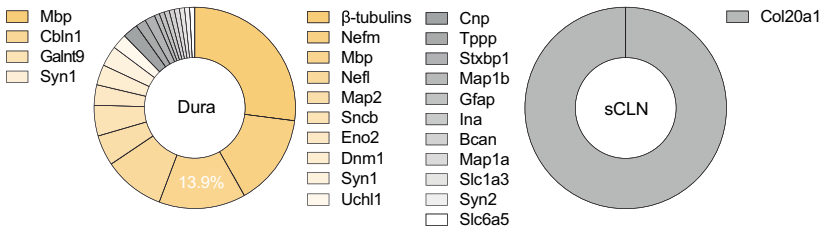
C57BL/6J males and females. Relative abundances (normalized peak areas) measured against a common identified peptide sequence, Dag1₄₈₈₋₅₃₁, from which relativity was ascertained. **e**, Venn diagram representation of individual CNS-enriched overlapping peptide sequences identified between C57BL/6J females and males in the dura. **f**, Bar graph showing the relative abundance of MBP peptides in the dura that comprised either the MBP₁₅₈₋₁₉₅ or MBP₁₉₆₋₂₃₆ regions in both C57BL/6J males and females. Relative abundances (normalized peak areas) measured against a common identified peptide sequence, Sptn1₃₈₁₋₃₈₉, from which relativity was determined.



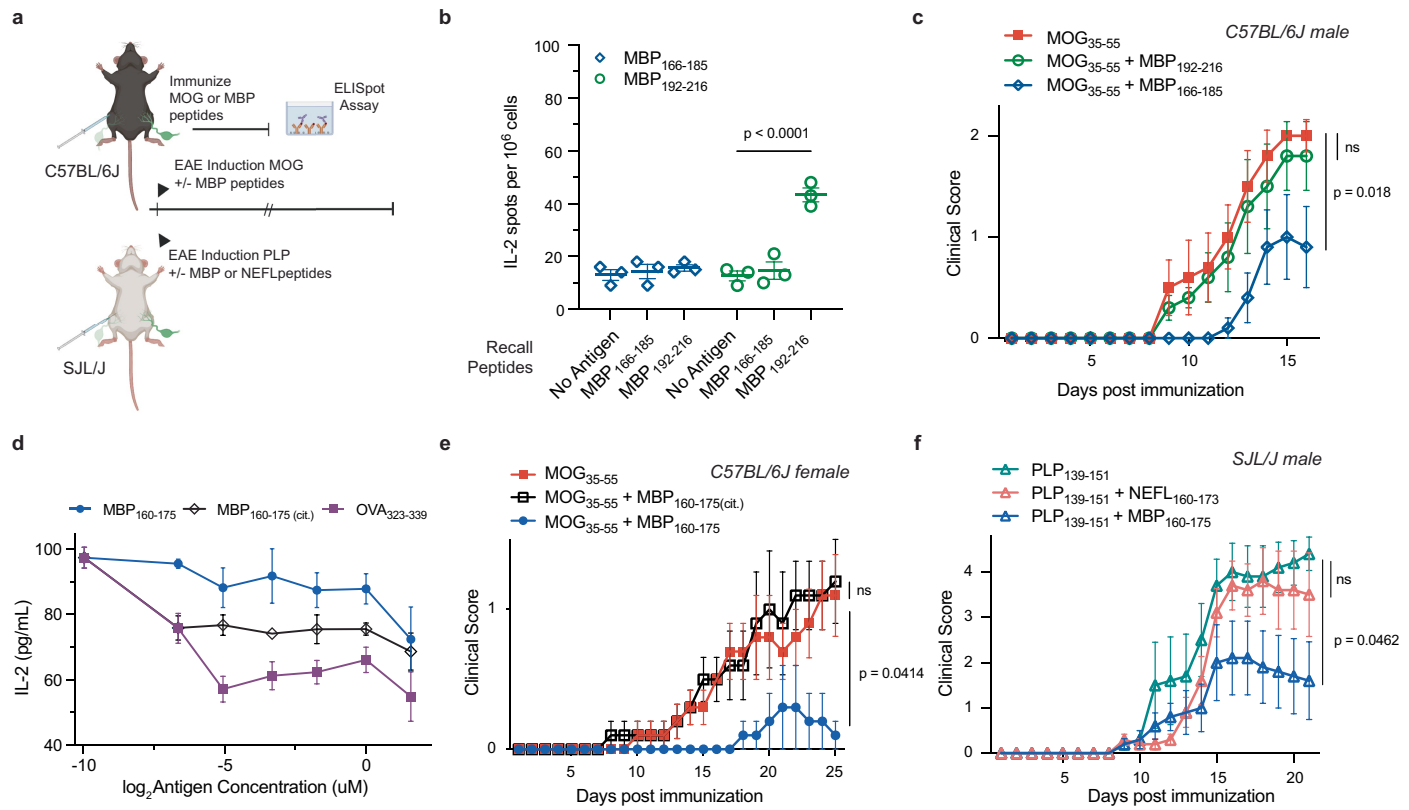
Extended Data Fig. 3 | The CNS MHC II peptidome of SJL/J male mice.

a, Violin plot depicting predicted binding affinities for unique MHC II-bound peptides in the brain (which also includes the leptomeninges), dura, dCLNs, and sCLNs of SJL/J mice. The median is represented by a solid line, and the first as well as the third quartiles are represented by dashed lines. P-values indicated on plot (one-way ANOVA with Tukey's multiple comparisons test). **b**, Evaluation of the proportion of total unique identified peptides designated as CNS enriched (teal bar) in the brain, dura, dCLNs, and sCLNs; percentages indicated above

each individual bar. **c-d**, Venn diagram illustrating the relationship between all peptides (**c**) or CNS-enriched peptides (**d**) bound to MHC II molecules across the different tissues in SJL/J male mice. **e**, Donut plot representation of all CNS-enriched peptides identified in the MHC II peptidome of SJL/J male mice for the brain, dura, and sCLNs. The part of the whole for which MBP represents is indicated in the plot, where relevant. **f**, Depiction of all individual peptide sequences deriving from MBP identified in the SJL/J male MHC II peptidome.

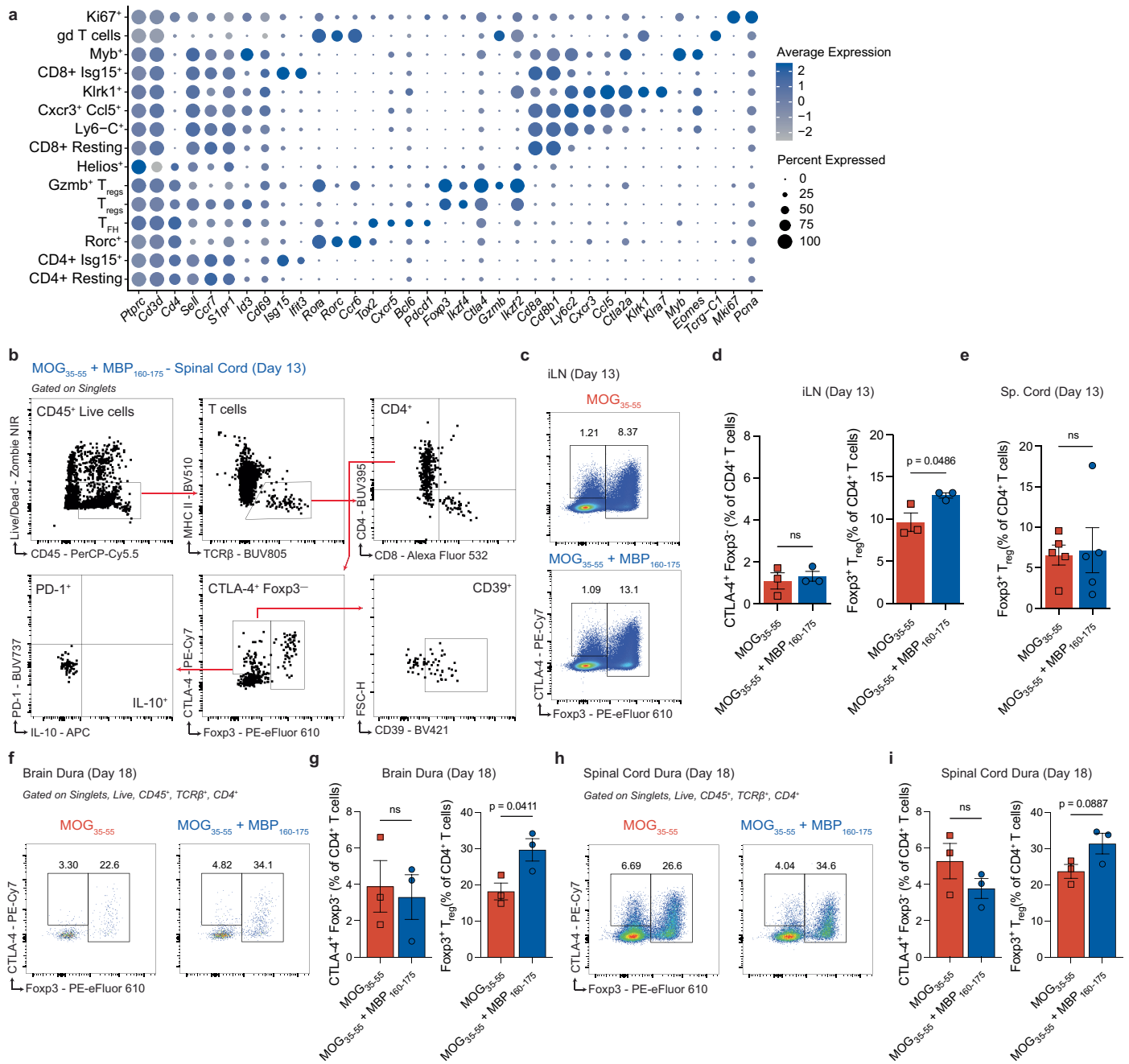


Article



Extended Data Fig. 4 | Endogenous regulatory MBP peptides protect across different models of neuroinflammation. **a**, Experimental design of C57BL/6J or SJL/J mice immunizations with MOG₃₅₋₅₅ or PLP₁₃₉₋₁₅₁ peptides, respectively, with or without MBP or NEFL peptides to actively induce EAE. Separately, C57BL/6J mice immunized with MOG or MBP peptides to perform ELISpot assay. Schematic created with BioRender.com. **b**, Mice immunized with MBP₁₆₆₋₁₈₅ or MBP₁₉₂₋₂₁₆ and ELISpot assay performed to measure IL-2 production upon recall with indicated peptides ($n = 3$ /group). Data shown as mean \pm s.e.m., two-way ANOVA with Šidák's post-hoc test performed. **c**, Average clinical EAE scores assessed by immunizing with MOG₃₅₋₅₅, MOG₃₅₋₅₅ + MBP₁₆₆₋₁₈₅ or MOG₃₅₋₅₅ + MBP₁₉₂₋₂₁₆ in C57BL/6J male mice ($n = 5$ /group). Plots display mean \pm s.e.m. and represent two independent experiments; two-way ANOVA with Dunnett's post-hoc test performed. **d**, Line graph representation of peptide competition

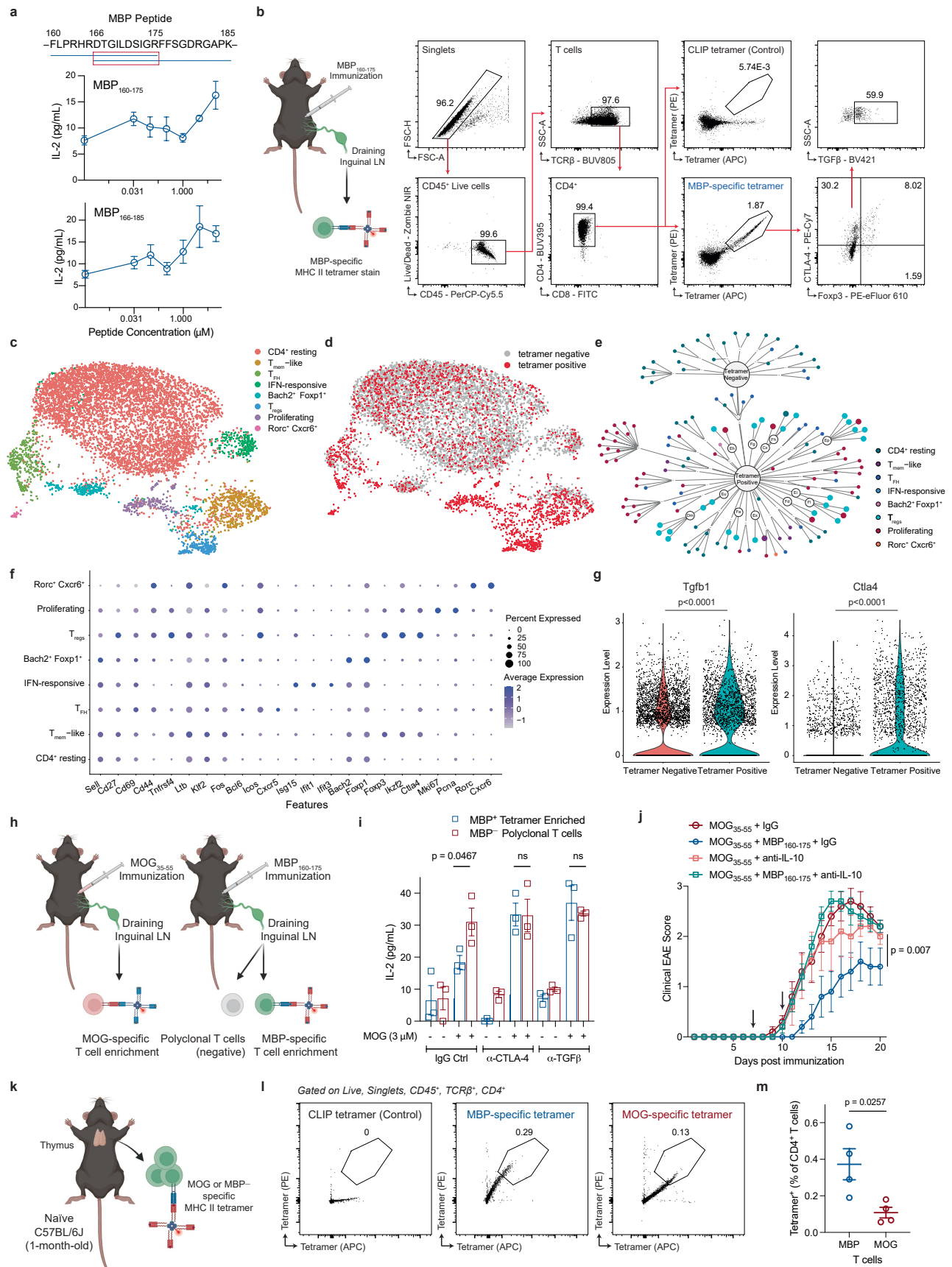
assay: dendritic cells, as APCs, incubated with varying doses of competitor peptides (MBP₁₆₀₋₁₇₅, MBP₁₆₀₋₁₇₅(cit.), OVA₃₂₃₋₃₃₉) and pulsed with a fixed concentration of MOG₃₅₋₅₅ antigen. Unbound peptides washed away and a MOG₃₅₋₅₅-specific hybridoma was introduced to assess its response by IL-2 ELISA. Plots shown as mean \pm s.e.m. and represent three independent experiments. **e**, Average clinical EAE scores assessed by immunizing with MOG₃₅₋₅₅, MOG₃₅₋₅₅ + MBP₁₆₀₋₁₇₅(cit.) or MOG₃₅₋₅₅ + MBP₁₆₀₋₁₇₅ in C57BL/6J female mice ($n = 5$ /group). Plots display mean \pm s.e.m. and represent three independent experiments; two-way ANOVA with Dunnett's post-hoc test used. **f**, Average clinical EAE scores assessed by immunizing with PLP₁₃₉₋₁₅₁, PLP₁₃₉₋₁₅₁ + MBP₁₆₀₋₁₇₅ or PLP₁₃₉₋₁₅₁ + NEFL₁₆₀₋₁₇₃ in SJL/J male mice ($n = 5$ /group). Plots display mean \pm s.e.m. and represent two independent experiments; two-way ANOVA with Dunnett's post-hoc test performed.



Extended Data Fig. 5 | Peripheral presentation of MBP peptides induces suppressor T cells. **a**, Dot plot of population markers from single cell RNA-sequencing scaled by percentage of cells expressing marker genes for each T cell cluster. **b**, Representative gating strategy for flow cytometry used to define within CD4⁺ T cells, CTLA-4⁺Foxp3⁻ T cells as well as conventional Foxp3⁺ regulatory T cells (T_{reg}). CTLA-4⁺Foxp3⁻ CD4⁺ T cells further gated to assess CD39, PD-1 (CD279), and IL-10 expression. **c-d**, Representative flow cytometry plots (**c**) with relevant quantifications (**d**) demonstrating the proportion of CTLA-4⁺Foxp3⁻ T cells and Foxp3⁺ T_{reg} within the CD4⁺ T cell population in the draining (inguinal) lymph nodes (iLN) 13 days post-immunization ($n=3$ /group, mean \pm s.e.m, unpaired two-tailed Student's t-test). **e**, Quantification of

conventional Foxp3⁺ T_{reg} as a frequency of CD4⁺ T cells in the spinal cord 13 days post-immunization ($n=5$ /group, mean \pm s.e.m, unpaired two-tailed Student's t-test). **f-g**, Representative flow cytometry plots (**f**) with quantifications (**g**) demonstrating the proportion of CTLA-4⁺Foxp3⁻ T cells and Foxp3⁺ T_{reg} within the CD4⁺ T cell population in the brain dura 18 days post-immunization ($n=3$ /group, mean \pm s.e.m, unpaired two-tailed Student's t-test). **h-i**, Representative flow cytometry plots (**h**) with quantifications (**i**) demonstrating the proportion of CTLA-4⁺Foxp3⁻ T cells and Foxp3⁺ T_{reg} within the CD4⁺ T cell population in the spinal cord dura 18 days post-immunization ($n=3$ /group, mean \pm s.e.m, unpaired two-tailed Student's t-test).

Article

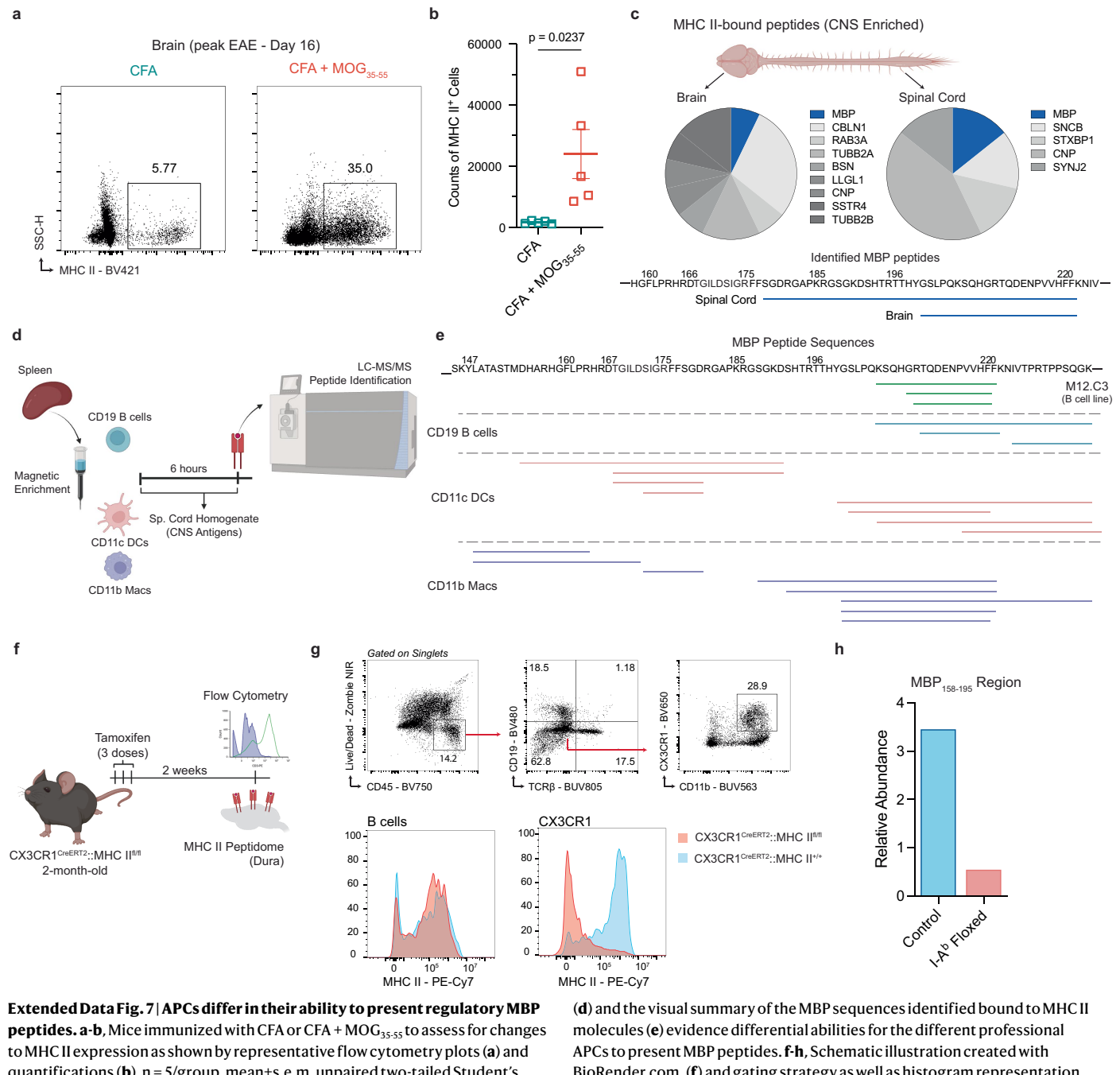


Extended Data Fig. 6 | See next page for caption.

Extended Data Fig. 6 | MBP-specific CD4⁺ T cells exhibit immunosuppressive capacity. **a**, Dose-response curve demonstrating reactivity of an MBP-specific hybridoma clone to MBP₁₆₀₋₁₇₅ and MBP₁₆₆₋₁₈₅ peptides; readout by IL-2 ELISA of half-logarithmic serial dilutions. Plots display mean±s.e.m and represent two independent experiments. **b**, Schematic created with BioRender.com. Gating strategy used to define MBP-specific CD4⁺ T cells by tetramer staining. **c-d**, CD4⁺ T cells isolated from draining iLNs after immunization with MBP₁₆₀₋₁₇₅; sorted for tetramer positive (MBP-specific) and tetramer negative CD4⁺ T cells. UMAP visualization depicts 8 CD4⁺ T cell subclusters (**c**) with enrichment to the T_{regs} subcluster in tetramer positive cells, indicated by red dots (**d**). **e**, Q-plot of TCR clones identified in tetramer negative (top) and tetramer positive (bottom) T cells colour-coded to represent the CD4⁺ T cell subcluster. **f**, Dot plot of population markers from scRNA-seq scaled by percentage of cells expressing marker genes for each CD4⁺ T cell cluster. **g**, Violin plot comparing *Tgfb1* and *Ctla4* expression between tetramer negative and tetramer positive samples.

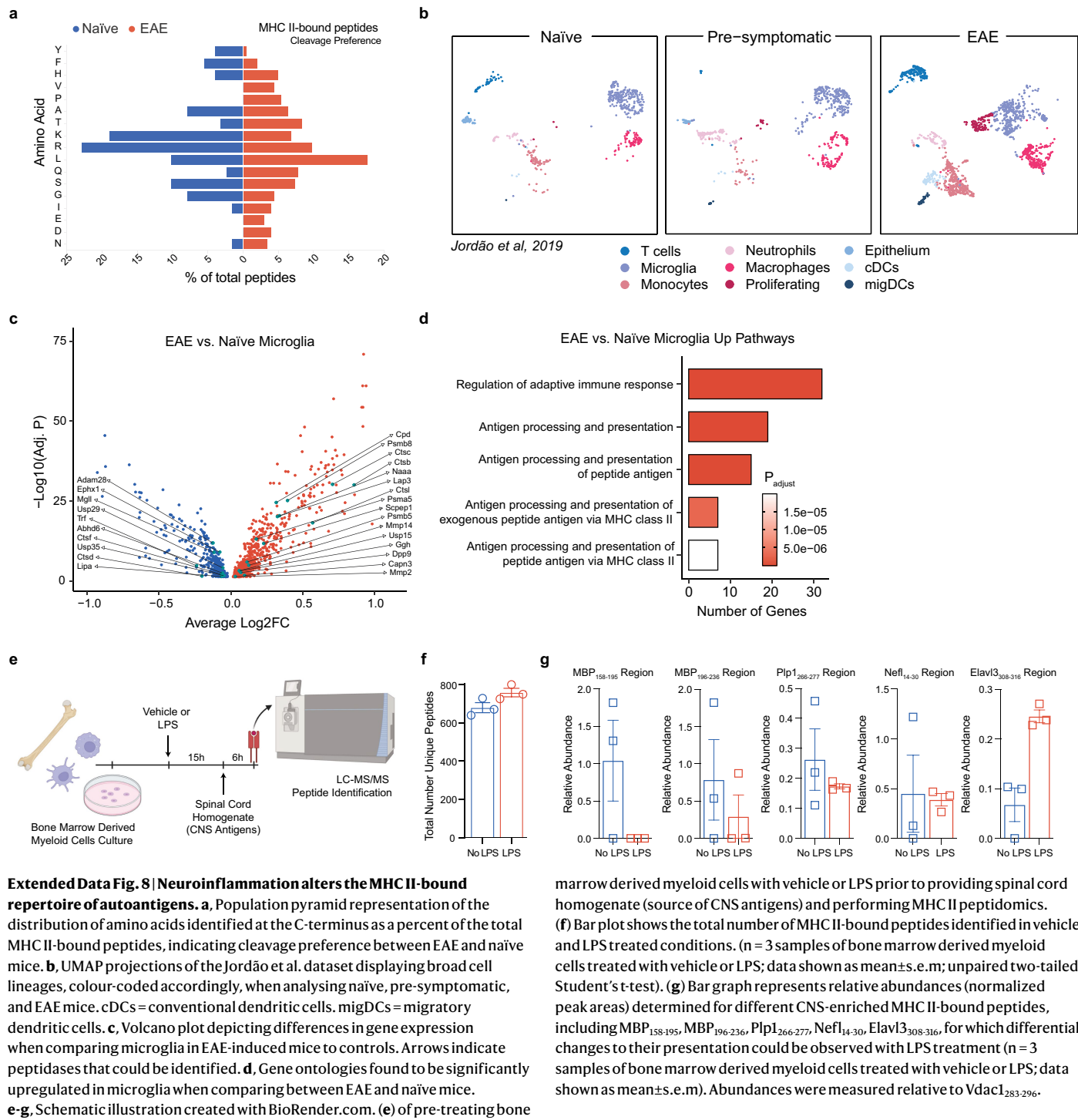
Data shown as mean±s.e.m (n = 8/group, unpaired two-tailed Student's t-test). **h-i**, Schematic created with BioRender.com. (**h**) and bar plot of IL-2 ELISA (**i**), demonstrating the attenuation of primary MOG-specific CD4⁺ T cell responses by primary MBP-specific CD4⁺ T cells but not by tetramer negative polyclonal CD4⁺ T cells; this was blunted by anti-CTLA-4 or anti-TGF β neutralizing antibodies. Data (mean±s.e.m) represent two independent experiments; two-way ANOVA performed. **j**, EAE assessed in mice immunized with MOG₃₅₋₅₅ or MOG₃₅₋₅₅ + MBP₁₆₀₋₁₇₅; on days 7 and 10 post-immunization, mice were treated with isotype control or anti-IL-10 neutralizing antibodies (n = 5/group). Data (mean±s.e.m) represent three independent experiments; two-way ANOVA with Dunnett's post-hoc test used. **k-m**, Schematic generated with BioRender.com. (**k**), representative flow cytometry plots (**l**), and quantifications (**m**) of tetramer staining of MBP-specific or MOG-specific CD4⁺ T cells in the thymus of naïve 1-month-old C57BL/6J mice (n = 4/group, mean±s.e.m, unpaired two-tailed Student's t-test).

Article



Extended Data Fig. 7 | APCs differ in their ability to present regulatory MBP peptides. **a-b**, Mice immunized with CFA or CFA + MOG₃₅₋₅₅ to assess for changes to MHC II expression as shown by representative flow cytometry plots (**a**) and quantifications (**b**, n = 5/group, mean ± s.e.m., unpaired two-tailed Student's t-test). **c**, Pie chart depiction of CNS-enriched, MHC II-bound peptides identified in the brain and spinal cord at the peak of EAE disease. Below is a visual summary of individual MBP sequences identified. Top image created with BioRender.com. **d-e**, Different professional antigen presenting cells (APCs), including CD19⁺ B cells, CD11c⁺ dendritic cells (DCs), and CD11b⁺ macrophages (Macs), were enriched from the spleens of naïve C57BL/6J mice. Spinal cord homogenate, a source of CNS antigens, was provided prior to the identification of MHC II-bound peptides by mass spectrometry. Schematic was created with BioRender.com.

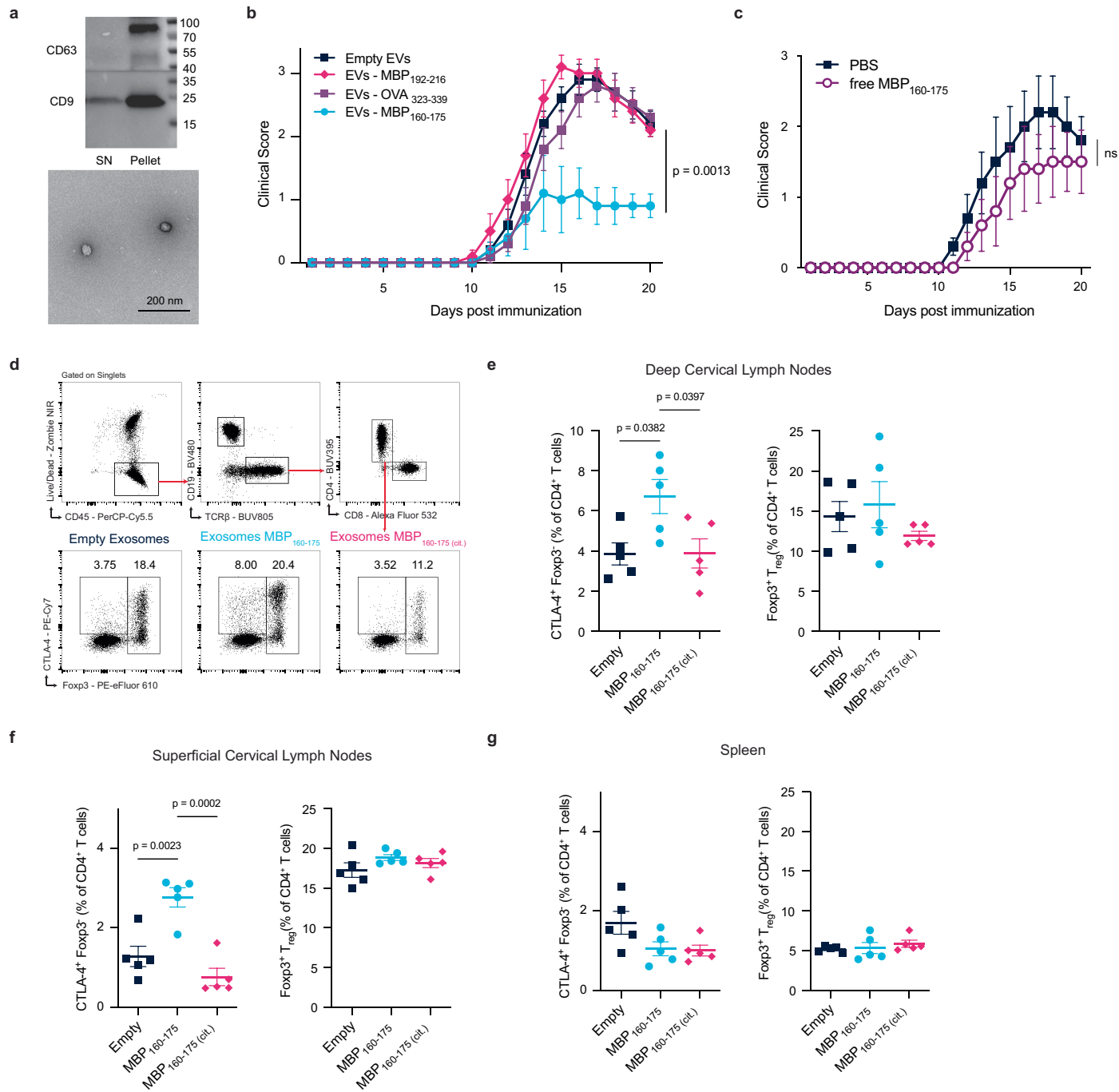
(d) and the visual summary of the MBP sequences identified bound to MHC II molecules (**e**) evidence differential abilities for the different professional APCs to present MBP peptides. **f-h**, Schematic illustration created with BioRender.com. (**f**) and gating strategy as well as histogram representation of MHC II expression (**g**) demonstrating the conditional ablation of MHC II molecules specifically on CX3CR1⁺ CD11b⁺ macrophages in the dural meninges with tamoxifen treated *Cx3cr1*^{CreERT2};H2-Ab1^{fl/fl} mice but not in control *Cx3cr1*^{CreERT2};H2-Ab1^{+/+} mice. (**h**) Relative abundances (normalized peak areas) of MHC II-bound peptides contained within the MBP₁₅₈₋₁₉₅ region in the dura, revealing a decrease with the loss of MHC II expression on CX3CR1⁺ CD11b⁺ macrophages; abundances were measured relative to Sptan1₃₈₁₋₃₈₉.



Extended Data Fig. 8 | Neuroinflammation alters the MHC II-bound repertoire of autoantigens. **a**, Population pyramid representation of the distribution of amino acids identified at the C-terminus as a percent of the total MHC II-bound peptides, indicating cleavage preference between EAE and naïve mice. **b**, UMAP projections of the Jordão et al. dataset displaying broad cell lineages, colour-coded accordingly, when analysing naïve, pre-symptomatic, and EAE mice. cDCs = conventional dendritic cells. migDCs = migratory dendritic cells. **c**, Volcano plot depicting differences in gene expression when comparing microglia in EAE-induced mice to controls. Arrows indicate peptidases that could be identified. **d**, Gene ontologies found to be significantly upregulated in microglia when comparing between EAE and naïve mice. **e-g**, Schematic illustration created with BioRender.com. (**e**) of pre-treating bone

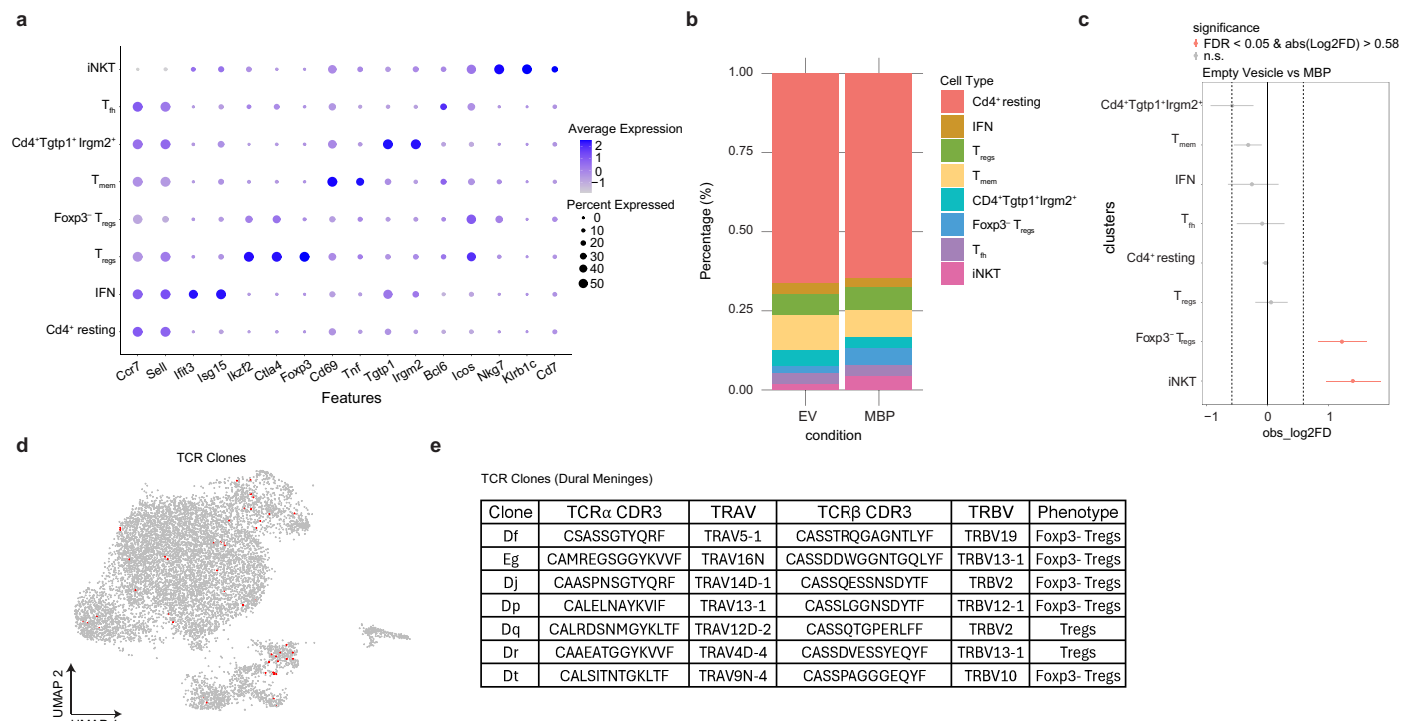
marrow derived myeloid cells with vehicle or LPS prior to providing spinal cord homogenate (source of CNS antigens) and performing MHC II peptidomics. (**f**) Bar plot shows the total number of MHC II-bound peptides identified in vehicle and LPS treated conditions. (n = 3 samples of bone marrow derived myeloid cells treated with vehicle or LPS; data shown as mean±s.e.m; unpaired two-tailed Student's t-test). (**g**) Bar graph represents relative abundances (normalized peak areas) determined for different CNS-enriched MHC II-bound peptides, including MBP₁₅₈₋₁₉₅, MBP₁₉₆₋₂₃₆, Pip1₂₆₆₋₂₇₇, Nefl₁₄₋₃₀, Elavl3₃₀₈₋₃₁₆, for which differential changes to their presentation could be observed with LPS treatment (n = 3 samples of bone marrow derived myeloid cells treated with vehicle or LPS; data shown as mean±s.e.m). Abundances were measured relative to Vdaci₂₈₃₋₂₉₆.

Article



Extended Data Fig. 9 | Delivery of encapsulated MBP peptides directly into the CSF induces suppressor CD4⁺ T cells. **a**, Immunoblot performed on the supernatant (SN) and resuspended pellet after ultracentrifugation evidencing enrichment of tetraspanins, CD9 and CD63, markers of extracellular vesicles (EVs). Blots represent two independent experiments. Below is a negative stain by transmission electron microscopy depicting enriched EVs, scale bar indicated on the panel. **b**, Mice were immunized with MOG₃₅₋₅₅ peptide and provided empty EVs, MBP₁₉₂₋₂₁₆ EVs, OVA₃₂₃₋₃₃₉ EVs, or MBP₁₆₀₋₁₇₅ EVs via i.c.m. injection on day 7 post immunization to induce EAE. Clinical EAE scores were tracked up to 20 days post immunization ($n = 5$ /group). Plots display mean \pm s.e.m and represent two independent experiments; two-way ANOVA with Dunnett's post-hoc test performed. **c**, Mice were immunized with MOG₃₅₋₅₅ to induce EAE after which they were provided with PBS or free MBP₁₆₀₋₁₇₅

peptides via i.c.m. injection on day 7. Average clinical EAE scores assessed until day 20 post immunization ($n = 5$ /group). Plots display mean \pm s.e.m and represent two independent experiments; two-way ANOVA with Dunnett's post-hoc test performed. **d**, Gating strategy for flow cytometry analysis to define within CD4⁺ T cells, CTLA-4⁺Foxp3⁻ unconventional suppressor T cells as well as conventional Foxp3⁺ T_{reg}. Representative flow cytometry plots of the dCLNs depicting gates for these populations with i.c.m. injection of empty EVs, MBP₁₆₀₋₁₇₅ EVs, or MBP₁₆₀₋₁₇₅(cit.) EVs. **e-g**, Quantification of unconventional CTLA-4⁺Foxp3⁻ suppressor T cells as well as conventional Foxp3⁺ T_{reg} as a frequency of CD4⁺ T cells of the deep cervical lymph nodes (**e**), superficial cervical lymph nodes (**f**), and spleen (**g**) ($n = 5$ /group, mean \pm s.e.m, one-way ANOVA with Tukey's post-hoc test).



Extended Data Fig. 10 | scRNA-seq of the CNS after local delivery of MBP peptides reveal expanded suppressor Foxp3 T cells. **a**, Dot plot of population markers from scRNA-seq scaled by percentage of cells expressing marker genes for each CD4+ T cell clusters. **b**, Bar graph representation of the proportion of CD4+ T cell clusters found in mice treated via intracisternal injection of either empty vesicles (EV) or MBP-containing vesicles (MBP). **c**, Log₂ fold change evaluated for the identified CD4+ T cell clusters by scRNA-seq

when comparing between mice that received intracisternal injection of empty vesicles or MBP-containing vesicles. Significant differences indicated on the plot ($n = 10/\text{group}$; data shown as mean \pm s.e.m.). **d**, UMAP visualization of T cell clonality of CD4+ T cells in mice that received MBP-containing vesicles. **e**, Tabulated depiction of CD4+ T cell clones of regulatory phenotypes identified in mice treated with MBP-containing vesicles – describing their TCR subtype, CDR3 sequences, and phenotype.

Corresponding author(s): Jonathan Kipnis

Last updated by author(s): October 15, 2024

Reporting Summary

Nature Portfolio wishes to improve the reproducibility of the work that we publish. This form provides structure for consistency and transparency in reporting. For further information on Nature Portfolio policies, see our [Editorial Policies](#) and the [Editorial Policy Checklist](#).

Statistics

For all statistical analyses, confirm that the following items are present in the figure legend, table legend, main text, or Methods section.

n/a Confirmed

- The exact sample size (n) for each experimental group/condition, given as a discrete number and unit of measurement
- A statement on whether measurements were taken from distinct samples or whether the same sample was measured repeatedly
- The statistical test(s) used AND whether they are one- or two-sided
Only common tests should be described solely by name; describe more complex techniques in the Methods section.
- A description of all covariates tested
- A description of any assumptions or corrections, such as tests of normality and adjustment for multiple comparisons
- A full description of the statistical parameters including central tendency (e.g. means) or other basic estimates (e.g. regression coefficient) AND variation (e.g. standard deviation) or associated estimates of uncertainty (e.g. confidence intervals)
- For null hypothesis testing, the test statistic (e.g. F , t , r) with confidence intervals, effect sizes, degrees of freedom and P value noted
Give P values as exact values whenever suitable.
- For Bayesian analysis, information on the choice of priors and Markov chain Monte Carlo settings
- For hierarchical and complex designs, identification of the appropriate level for tests and full reporting of outcomes
- Estimates of effect sizes (e.g. Cohen's d , Pearson's r), indicating how they were calculated

Our web collection on [statistics for biologists](#) contains articles on many of the points above.

Software and code

Policy information about [availability of computer code](#)

Data collection

The following softwares were used for data collection in this study:

- Thermo Scientific Orbitrap Fusion Lumos Control Software
- Illumina NextSeq Control Software
- CYTEK SpectroFlo
- Bio-Rad Image Lab
- BioTek Gen5 3.11
- CTL ImmunoSpot S6 Universal
- Cellranger_1.1.0

Data analysis

The following softwares were used for data analysis in this study:

- PEAKS Studio 10.6
- Prism v9.5.1
- FlowJo v10.9.0
- ImmunoSpot Professional 6.0.0
- R v3.5.0
- 10x genomics Cellranger software pipeline
- Seurat v3
- Custom code used for single-cell RNA-seq analysis will be made available upon reasonable request by the corresponding author.

For manuscripts utilizing custom algorithms or software that are central to the research but not yet described in published literature, software must be made available to editors and reviewers. We strongly encourage code deposition in a community repository (e.g. GitHub). See the Nature Portfolio [guidelines for submitting code & software](#) for further information.

Data

Policy information about [availability of data](#)

All manuscripts must include a [data availability statement](#). This statement should provide the following information, where applicable:

- Accession codes, unique identifiers, or web links for publicly available datasets
- A description of any restrictions on data availability
- For clinical datasets or third party data, please ensure that the statement adheres to our [policy](#)

Human Protein Atlas Database (<https://www.proteinatlas.org>)

MEROPS peptidase database (<https://www.ebi.ac.uk/merops/>)

Adventitious Proteins database (www.thegpm.org/crap/)

Raw mass spectrometry data and peptide-spectrum matches have been deposited in the MassIVE public proteomics repository (<http://massive.ucsd.edu>) with the identifier MSV000092643 and are available at <ftp://massive.ucsd.edu/MSV000092643>. Single-cell RNA sequencing is available at the Gene Expression Omnibus under accession GSE240691, GSE272901, GSE273051, GSE276987.

Research involving human participants, their data, or biological material

Policy information about studies with [human participants or human data](#). See also policy information about [sex, gender \(identity/presentation\), and sexual orientation](#) and [race, ethnicity and racism](#).

Reporting on sex and gender

N/A

Reporting on race, ethnicity, or other socially relevant groupings

N/A

Population characteristics

N/A

Recruitment

N/A

Ethics oversight

N/A

Note that full information on the approval of the study protocol must also be provided in the manuscript.

Field-specific reporting

Please select the one below that is the best fit for your research. If you are not sure, read the appropriate sections before making your selection.

Life sciences

Behavioural & social sciences

Ecological, evolutionary & environmental sciences

For a reference copy of the document with all sections, see nature.com/documents/nr-reporting-summary-flat.pdf

Life sciences study design

All studies must disclose on these points even when the disclosure is negative.

Sample size

Sample sizes, where necessary, were selected based on a standard power calculation ($\alpha=0.05$, power of 0.8). Generally, statistical methods were not used to recalculate or to predetermine sample sizes but were based on similar experiments published previously (Rustenhoven et al., *Cell* (2021); Louveau et al., *Nat Neurosci* (2018)).

Data exclusions

No data were excluded for analysis.

Replication

Experiments were replicated in at least two independent experiments of at least 3, but often 5 mice per group; this information is provided in the figure legends. All data were successfully reproduced. For single cell sequencing, mice (number mentioned in manuscript) were pooled in each group and sequenced together. Similarly, for immunopeptidomics, mice (number mentioned in manuscript) were pooled and processed together for analysis by liquid chromatography tandem mass spectrometry.

Randomization

Cages, containing no more than 5 mice, were randomly assigned to the different experimental groups. All variables were controlled for. As such, no covariates were present.

Blinding

For single cell sequencing, the analyzer performed the analysis blinded. For EAE, clinical scoring was performed daily by the experimenter, who was kept blinded to the identity of the groups, until the data was collected and analyzed. For other experiments, including immunopeptidomics, in vitro cell culture studies, among others, no blinding was performed to prevent any cross-contamination between groups.

Reporting for specific materials, systems and methods

We require information from authors about some types of materials, experimental systems and methods used in many studies. Here, indicate whether each material, system or method listed is relevant to your study. If you are not sure if a list item applies to your research, read the appropriate section before selecting a response.

Materials & experimental systems

n/a	Involved in the study
<input type="checkbox"/>	<input checked="" type="checkbox"/> Antibodies
<input type="checkbox"/>	<input checked="" type="checkbox"/> Eukaryotic cell lines
<input checked="" type="checkbox"/>	<input type="checkbox"/> Palaeontology and archaeology
<input type="checkbox"/>	<input checked="" type="checkbox"/> Animals and other organisms
<input checked="" type="checkbox"/>	<input type="checkbox"/> Clinical data
<input checked="" type="checkbox"/>	<input type="checkbox"/> Dual use research of concern
<input checked="" type="checkbox"/>	<input type="checkbox"/> Plants

Methods

n/a	Involved in the study
<input checked="" type="checkbox"/>	<input type="checkbox"/> ChIP-seq
<input type="checkbox"/>	<input checked="" type="checkbox"/> Flow cytometry
<input checked="" type="checkbox"/>	<input type="checkbox"/> MRI-based neuroimaging

Antibodies

Antibodies used

CD11b BUV563 (741242, BD Biosciences), CD11c BUV737 (749039, BD Biosciences), CD19 BV480 (566107, BD Biosciences), CD25 Alexa Fluor 700 (102024, BioLegend), CD25 Pacific Blue (102022, BioLegend), CD39 BV421 (567105, BD Biosciences), CD4 BUV395 (740208, BD Biosciences), CD44 BUV615 (751414, BD Biosciences), CD45 BV750 (746947, BD Biosciences), CD45 PerCP-Cy5.5 (550994, eBioscience), CD8a Alexa Fluor 532 (58-0081-80, eBioscience), CD8a APC-eFluor 780 (47-0081-82, eBioscience), CD8a FITC (11-0081-82, eBioscience), CTLA-4 PE-Cy7 (106314, BioLegend), F4/80 Alexa Fluor 700 (123130, BioLegend), Foxp3 PE-eFluor610 (61-5773-82, Invitrogen), ROR γ BV650 (564722, BD Biosciences), T-bet PE-Cy7 (25-5825-82, eBioscience), Granzyme B PE-Cy5 (372226, BioLegend), IL-10 APC (554468, BD Biosciences), LAP (TGF- β 1) BV421 (141408, BioLegend), MHC II PE-Cy7 (25-5321-82, eBioscience), MHC II BV510 (107635, BioLegend), MHC II BV421 (107631, BioLegend), PD-1 BUV737 (749306, BD Biosciences), CD200 BV786 (744653, BD Biosciences), CD27 BUV563 (741271, BD Biosciences), TCR β BUV805 (748405, BD Biosciences), Ly6G BUV661 (741587, BD Biosciences), Ly6C BV510 (128033, BioLegend), Thy1.2 Alexa Fluor 647 (105318, BioLegend), TCR β PE (109208, BioLegend), Zombie NIR Fixable Viability Kit (423106, BioLegend), CD16/CD32 (Fc Block) (101302, BioLegend) were used for flow cytometry experiments.
AffiPure Normal Mouse IgG (Leinco, N229-6850-8800) and anti-mouse MHC class II (I-A) (BioXCell, BE0178) used to isolate peptides for the MHC II peptidomes.
Mouse IL-2 ELISpot Pair (BD Biosciences, 551876) are capture and detection IL-2 antibodies used for ELISpot experiments.
CD9 (124802, BioLegend) and CD63 (143901, BioLegend) are antibodies used for immunoblots. IL-2 ELISA performed by using the provided capture and detection antibodies provided in the Mouse IL-2 ELISA Ready SET Go! Kit (88702476, eBioscience).
Neutralizing antibodies used in EAE experiments include, anti-CTLA-4 (BE0131, Bio X Cell), anti-TGF β (BE0057, Bio X Cell), and anti-IL-10 (BE0049, Bio X Cell).

Validation

Antibodies listed above were validated for species and application (flow cytometry, immunopurification, immunoblot, and fluorescence activated cell sorting) by the corresponding manufacturer. Usage are detailed in full in the manuscript. Furthermore, all antibodies were assessed with control tissues, including spleen, blood, among others, prior to use in experimentation.

Eukaryotic cell lines

Policy information about [cell lines and Sex and Gender in Research](#)

Cell line source(s)

DC2.4 cell line (CVCL_J409) was purchased from the American Type Culture Collection (ATCC). M12.C3 (H2-Ab-expressing) was provided as a gift by X. Wan (Department of Pathology and Immunology, Washington University in St. Louis, St. Louis, MO). CD4+ T cell hybridomas were generated in the laboratory.

Authentication

Identity of cell line assessed by checking morphological features routinely, after initially acquiring the cell lines, short tandem repeat (STR) profiling was not performed thereafter.

Mycoplasma contamination

Cell morphology was frequently assessed but mycoplasma contamination was not assessed as frequently by PCR.

Commonly misidentified lines (See [ICLAC](#) register)

No commonly misidentified cell lines are employed in this study.

Animals and other research organisms

Policy information about [studies involving animals; ARRIVE guidelines](#) recommended for reporting animal research, and [Sex and Gender in Research](#)

Laboratory animals

C57BL/6J (WT, 8-12 weeks old; JAX000664) and SJL/J (WT, 8-12 weeks old; JAX000686) were purchased from the Jackson Laboratory. Cx3cr1-CreERT2 mice were available prior in the lab and can be purchased through the Jackson Laboratory. MHC II fl/fl mice were provided as a gift by K. Murphy (Department of Pathology and Immunology, Washington University in St. Louis, St. Louis, MO). All

mice were maintained in standard housing conditions (temperature at 22°C, humidity maintained between 33-39%, 12 hour light/dark cycle and provided with sterilized water and regular rodent chow ad libitum unless stated otherwise). Mice were allowed to acclimate for at least one week in the animal facility prior to the beginning of any experiment.

Wild animals	No wild animals involved as part of this study.
Reporting on sex	Both adult males and females between 8-12 weeks of age were used for our studies unless stated otherwise.
Field-collected samples	No collection of samples from the field utilized for this study.
Ethics oversight	All experiments were approved by the Institutional Animal Care and Use Committee at the Washington University in St. Louis.

Note that full information on the approval of the study protocol must also be provided in the manuscript.

Flow Cytometry

Plots

Confirm that:

- The axis labels state the marker and fluorochrome used (e.g. CD4-FITC).
- The axis scales are clearly visible. Include numbers along axes only for bottom left plot of group (a 'group' is an analysis of identical markers).
- All plots are contour plots with outliers or pseudocolor plots.
- A numerical value for number of cells or percentage (with statistics) is provided.

Methodology

Sample preparation

Mice were injected with lethal dose of Euthasol intraperitoneally. Mice were then perfused by transcardial perfusion with PBS containing heparin (0.025%); samples were collected into ice-cold RPMI and maintained on ice for the entirety of tissue collection. Spleens were digested and mashed through a 70 µm cell strainer with a glass pestle and washed with 5 mL of RPMI. Cells were then centrifuged at 450g for 5 minutes. RBC lysis was performed with 1 mL of ACK lysis buffer (Quality Biological); cells were incubated for 2 minutes and then 2 mL of ice-cold PBS was supplemented to the sample. Samples were subsequently centrifuged at 450g for 5 minutes and lysed red blood cells were aspirated. Thymi and lymph nodes were similarly digested and mashed through a 70 µm cell strainer, washed with 2 mL RPMI, centrifuged, resuspended in FACS buffer, and kept on ice until further use. Choroid plexus removed from the brain; similarly, the dural meninges were peeled from the skull cap using Dumont #5 forceps (Fine Science Tools). Dural meninges were digested for 15 minutes at 37°C with constant agitation using 1 mL of pre-warmed digestion buffer (RPMI-1640 medium with 2% FBS, 1 mg/mL Collagenase VIII, and 0.5 mg/mL DNase I). They were then filtered through a 70 µm cell strainer and provided with 1 mL of complete medium (RPMI with 10% FBS) to neutralize the enzymes. Samples were then centrifuged at 450g for 5 minutes, resuspended in FACS buffer and kept on ice. Lastly, brains and spinal cords were mechanically dissociated using sterile surgical scalpels into ~1 mm³ cubes and digested with constant agitation in 2 mL of pre-warmed digestion buffer for 20 minutes at 37°C, triturated with a 10 mL serological pipette, digested for another 20 minutes, triturated with a 5 mL serological pipette, and digested for an additional 20 minutes. To remove myelin, a 1:1 ratio of 22% bovine serum albumin (BSA) in PBS was added and centrifuged at 1000g for 10 minutes. Following centrifugation, the floating myelin layer was aspirated. Cell pellets were then neutralized with RPMI with 10% FBS to halt the enzymatic digestion. An additional 5 mL of RPMI with 10% FBS was added to wash the pellet. Samples were centrifuged at 450g for 5 minutes, resuspended in FACS buffer (2% BSA, 1 mM ethylenediamine acetic acid (EDTA), 20 mM HEPES). Further enrichment for antigen presenting cells prior to immunopeptidomics were performed on single cell suspensions isolated from the spleen; CD19+ B cells enriched using the EasySep Mouse B cell Isolation Kit (NC0378722, STEMCELL Technologies), CD11c+ dendritic cells using the CD11c MicroBeads UltraPure, mouse (130-125-835, Miltenyi Biotec) and CD11b+ macrophages using the CD11b MicroBeads UltraPure, mouse (130-126-725, Miltenyi Biotec). For bone marrow derived myeloid cell cultures, femurs were isolated from naïve mice and flushed in sterile conditions. They were provided with RPMI full medium (RPMI-1650 medium with 10% FBS, 1% penicillin/streptomycin, 2 mM L-glutamine, and 50 µM β-mercaptoethanol) supplemented with GM-CSF (576304, BioLegend). If for MHC II tetramer staining, single cell suspensions were first enriched for CD4 T cells using the CD4 T cell isolation kit (19852, STEMCELL Technologies). Biotinylated MHC II monomers for either MOG(35-55) or MBP(160-175) were generated by the Dr. Likui Yang through the Bursky Center for Human Immunology & Immunotherapy Programs (CHiiPs). They were thereafter conjugated to Streptavidin-R-PE (PJRS25-1, Agilent Technologies) or to Streptavidin-APC (PJ27S-1, Agilent Technologies). The enriched CD4 T cells were then incubated with MHC II tetramers for 20 minutes at 37°C after which they were stabilized using anti-PE beads (130-048-801, Miltenyi Biotec) and anti-APC beads (130-090-855, Miltenyi Biotec). They were then stained for surface markers and further for intracellular markers as detailed below. If not for MHC II tetramer, single cell suspensions were incubated with Zombie NIR (BioLegend) diluted 1:800 in ice-cold PBS for 15 minutes at 4°C for viability staining. Samples were then subsequently centrifuged, resuspended in FACS buffer containing anti-CD16/32 (Fc block; BioLegend) diluted 1:100 in FACS buffer for 5 minutes. Cells were then stained for 30 minutes at 4°C for surface markers with antibodies diluted appropriately in FACS buffer. If requiring intracellular cytokine staining, samples were incubated in the presence of cell stimulation cocktail (50-930-5, eBioscience) and Brefeldin A solution (00-4506-51, eBioscience) for 4 hours at 37°C. For samples requiring intracellular staining, surface staining was performed first as described above. Then, cells were fixed and permeabilized using the Foxp3/Transcription Factor Staining Buffer Set (eBioscience); staining was performed for 30 minutes at 4°C with fluorescently conjugated antibodies against intracellular molecules. Samples were filtered prior with 70 µm cell strainer prior to data collection.

Instrument

Aurora Spectral Flow Cytometer (CYTEK)

Software

CYTEK SpectroFlo for data collection.
FlowJo v10.9.0 for data analysis.

Cell population abundance

Individual experiments all involved incubation of cell suspensions with viability dyes to ensure assessment of live cells. Control tissues used as well for gating. For cells sorted for sequencing, a small portion of the sorted T cells were reassessed by flow cytometry to confirm its purity.

Gating strategy

Gating strategies are provided in supplementary figures, where relevant.
But, briefly:
MHC II+ cells: Live, Singlets, CD45+, MHC II+
Macrophages: Live, Singlets, CD45+, MHC II+, CD19-, CD11c-, F4/80+, CD11b+
Dendritic cells: Live, Singlets, CD45+, MHC II+, CD19-, CD11c+
B cells: Live, Singlets, CD45+, MHC II+, CD19+, CD11c-
CD4+ T cells: Live, Singlets, CD45+, MHC II-, TCRβ+, CD4+, CD8-
Foxp3 Tregs: Live, Singlets, CD45+, MHC II-, TCRβ+, CD4+, CD8-, Foxp3+
Suppressor CD4 T cells: Live, Singlets, CD45+, MHC II-, TCRβ+, CD4+, CD8-, Foxp3-, CTLA-4+ (This population was further assessed for staining of CD39, IL-10, PD-1 (CD279).
Tetramer+ cells: Live, Singlets, CD45+, TCRβ+, CD4+, CD8-, Tetramer+ (This population was further assessed for staining of CTLA-4, Foxp3, TGFβ, IL-10, PD-1 (CD279).

Tick this box to confirm that a figure exemplifying the gating strategy is provided in the Supplementary Information.